The Astrophysical Journal, 773:15 (16pp), 2013 August 10 doi:10.1088/0004-637X/773/1/15
© 2013. The American Astronomical Society. All rights reserved. Printed in the U.S.A.

REVEALING THE HEAVILY OBSCURED ACTIVE GALACTIC NUCLEUS POPULATION OF HIGH-REDSHIFT 3CRR SOURCES WITH *CHANDRA* X-RAY OBSERVATIONS

Belinda J. Wilkes[1], Joanna Kuraszkiewicz[1], Martin Haas[2], Peter Barthel[3], Christian Leipski[4], S. P. Willner[1], D. M. Worrall[5], Mark Birkinshaw[5], Robert Antonucci[6], M. L. N. Ashby[1], Rolf Chini[2,7], G. G. Fazio[1], Charles Lawrence[8], Patrick Ogle[9], and Bernhard Schulz[10]

[1] Harvard-Smithsonian Center for Astrophysics, Cambridge, MA 02138, USA
[2] Astronomisches Institut, Ruhr-University, D-44801 Bochum, Germany
[3] Kapteyn Institute, University of Groningen, 9747 AD Groningen, The Netherlands
[4] MPIA, D-69117 Heidelberg, Germany
[5] H. H. Wills Physics Laboratory, University of Bristol, Bristol BS8 1TL, UK
[6] Department of Physics, University of California, Santa Barbara, CA 93106, USA
[7] Instituto de Astronomía, Universidad Católica del Norte, Antofagasta, Chile
[8] JPL, Pasadena, CA 91109, USA
[9] Spitzer Science Center, Caltech, Pasadena, CA 91125, USA
[10] IPAC, Caltech, Pasadena, CA 91125, USA
Received 2013 February 26; accepted 2013 May 30; published 2013 July 19

ABSTRACT

Chandra observations of a complete, flux-limited sample of 38 high-redshift ($1 < z < 2$), low-frequency-selected (and so unbiased in orientation) 3CRR radio sources are reported. The sample includes 21 quasars (=broad-line radio galaxies) and 17 narrow-line radio galaxies (NLRGs) with matched 178 MHz radio luminosity ($\log L_{\rm R}(5\,{\rm GHz}) \sim$ 44–45). The quasars have high radio core fraction, high X-ray luminosities ($\log L_{\rm X} \sim$ 45–46), and soft X-ray hardness ratios (HR ~ -0.5) indicating low obscuration. The NLRGs have lower core fraction, lower apparent X-ray luminosities ($\log L_{\rm X} \sim$ 43–45), and mostly hard X-ray hardness ratios (HR > 0) indicating obscuration ($N_{\rm H} \sim 10^{22}$–10^{24} cm^{-2}). These properties and the correlation between obscuration and radio core fraction are consistent with orientation-dependent obscuration as in unification models. About half the NLRGs have soft X-ray hardness ratios and/or a high [O III] emission line to X-ray luminosity ratio suggesting obscuration by Compton thick (CT) material so that scattered nuclear or extended X-ray emission dominates (as in NGC 1068). The ratios of unobscured to Compton-thin (10^{22} cm$^{-2} < N_{\rm H}({\rm int}) < 1.5 \times 10^{24}$ cm^{-2}) to CT ($N_{\rm H}({\rm int}) > 1.5 \times 10^{24}$ cm^{-2}) is 2.5:1.4:1 in this high-luminosity, radio-selected sample. The obscured fraction is 0.5, higher than is typically reported for active galactic nuclei at comparable luminosities from multi-wavelength surveys (0.1–0.3). Assuming random nuclear orientation, the unobscured half-opening angle of the disk/wind/torus structure is $\sim 60^\circ$ and the obscuring material covers 30°, $\sim 12^\circ$ of which is CT. The multi-wavelength properties reveal that many NLRGs have intrinsic absorption 10–1000× higher than indicated by their X-ray hardness ratios, and their true $L_{\rm X}$ values are ∼10–100× larger than the hardness-ratio absorption corrections would indicate.

Key words: quasars: general – X-rays: galaxies

Online-only material: color figures

1. INTRODUCTION

The standard model for the nuclear regions of an active galaxy (active galactic nucleus, AGN) includes a supermassive black hole (SMBH) surrounded by an accretion disk (AD) and a corona producing strong, thermal optical–UV–soft-X-ray and non-thermal X-ray emission. Gas and dust in the vicinity are heated by the nuclear emission producing the broad and narrow ultraviolet (UV), optical, and infrared (IR) emission lines, and the near-IR hot dust emission characteristic of AGNs. Radio-loud (RL) AGNs also include relativistic jets of plasma streaming outward from the nucleus along the AD axis and emitting non-thermal synchrotron and associated inverse-Compton radiation. The observed radio structures include jets, hot spots, and lobes for which the appearance (core/lobe dominated) is strongly related to the viewing angle/orientation of the source to our line of sight (Barthel 1989). AGNs are broadly classified into type 1 sources, with both broad and narrow UV–IR emission lines, and type 2 sources with only narrow emission lines. The detection of polarized broad lines in 3C 234 (Antonucci 1984) and NGC 1068 (Antonucci & Miller 1985) led to the general acceptance that some fraction of (narrow-lined) Seyfert 2s are absorbed, edge-on (broad-lined) Seyfert 1s, so that absorption and orientation are also factors for at least some radio-quiet AGNs (RQAGNs). The generally accepted unification model for AGNs (Barthel 1989; Antonucci & Miller 1985) interprets the observed range in emission lines, radio structures, and other properties as being primarily due to the orientation of the source relative to our line of sight.

As a result of the orientation dependence of their observational characteristics, a critical problem in understanding AGNs is to distinguish observed differences due to orientation from intrinsic physical differences. The AD and corona, possibly combined with a larger torus and/or wind (Elvis 2000; Konigl & Kartje 1994), provide obscuration which is anisotropic and strongly frequency dependent and results in complex, orientation-dependent selection effects for observations in most wavebands. This affects both source detection and classification. The orientation dependence of the observed spectral energy distributions (SEDs) of AGNs results in differing levels of bias against most obscured sources in traditional optical/ultraviolet/near-infrared/soft X-ray surveys. Orientation unbiased surveys, which would properly test unification schemes, are difficult to come by.

The advent of the Great Observatories has facilitated a number of major multi-wavelength surveys (e.g., SWIRE: Lonsdale et al. 2003; GOODS: Giavalisco et al. 2004; Boötes: Hickox et al. 2007; ChaMP: Kim et al. 2007; COSMOS: Scoville et al. 2007; AEGIS: Davis et al. 2007, Eisenhardt et al. 2004; CANDELS: Grogin et al. 2011; Koekemoer et al. 2011; HERMES: Oliver et al. 2012) which, through the use of hard X-ray and/or mid-infrared (IR) selection, probe the AGN population, including obscured objects, more completely than traditional surveys (Best et al. 2000; Polletta et al. 2006). Mid-IR selection requires secondary, usually X-ray selection to distinguish AGNs from the larger IR galaxy population (Donley et al. 2012; Polletta et al. 2006; Barmby et al. 2006), but even then a bias against highly obscured sources remains. Although incomplete, surveys at near-IR wavelengths (Two Micron All Sky Survey, 2MASS; Cutri et al. 2002; Martínez-Sansigre et al. 2005) have revealed a population of red, moderately obscured AGNs (Wilkes et al. 2002, 2005) of both types 1 and 2 with space density comparable to normal type 1 AGNs. Current cosmic X-ray background (CXRB) models successfully include approximately equal populations of unobscured and moderately obscured ($\log N_{\rm H}({\rm int}) \sim 21$–23) AGNs to model the emission up to ~10 keV (Gilli et al. 2007). However, a population of Compton thick (CT; $N_{\rm H} > 1.5 \times 10^{24}$ cm^{-2}) AGNs comparable to that of Compton thin AGNs is required to explain the higher energy (~30 keV) CXRB. This CT population remains mostly undetected individually. They are difficult to find, even at *Chandra* and *XMM-Newton* X-ray energies ($\lesssim$10 keV). Direct light from NGC 1068, the "Rosetta-stone" type 2 source, is undetected by *BeppoSAX*, i.e., to energies $\gtrsim$100 keV (Matt et al. 1997). Estimates, which are based on the small numbers found and/or on X-ray stacking techniques (Fiore et al. 2012, 2009; Daddi et al. 2007; Polletta et al. 2006; Tozzi et al. 2006; Bassani et al. 2006; Panessa et al. 2006; Cappi et al. 2006; Risaliti et al. 1999), cover a wide range (0.05− > 2× the rest of the AGN population).

Low-frequency radio selection, which is based on extended, optically thin emission and so is largely independent of orientation, provides the only way to assemble a complete, randomly oriented sample of AGNs. We are therefore carrying out a multi-wavelength study of a well-defined sample of low-frequency radio-selected (178 MHz), high-redshift ($1 < z < 2$), and thus high-luminosity ($\log L_{\rm R}(5\,{\rm GHz}) \sim 44$–45), 3CRR radio sources. A major advantage provided by the radio data is an independent orientation indicator in the relative strength of the (beamed) core and (isotropic) extended emission (core fraction $R_{\rm CD} = F_{\rm core}/F_{\rm lobe}(5\,{\rm GHz})$; Orr & Browne 1982). Models for the AGN nuclear obscuration range from geometrically thick, smooth (Krolik & Begelman 1988), or clumpy (Nenkova et al. 2008) tori to ADs with winds (Konigl & Kartje 1994; Elvis 2000) and/or warps (Lawrence & Elvis 2010). The key input of the X-ray absorption column densities, IR–optical SEDs, and radio core fraction can help to discriminate between and/or constrain these models.

One caveat to an RL sample is that only ~10% of AGNs are RL, and they may not accurately represent the majority AGN population, e.g., radio-emitting plasma may affect the opening angle of the torus (Falcke et al. 1995), and generally the X-ray emission includes an extra extended component related to the radio core and jet.

1.1. X-Rays from Radio-loud Quasars

The X-ray emission from RQAGNs is well known to include multiple components (Mushotzky et al. 1993). As well as the non-thermal, accretion-related power law which dominates the X-ray emission of luminous broad-lined AGNs, contributions from a soft excess, generally linked to the AD, reflected emission from hot and/or cold material surrounding the nucleus, emission lines (Ogle et al. 2003), and/or scattered nuclear light become significant in lower-luminosity sources and at high inclinations when the nuclear light is strongly obscured (Mushotzky et al. 1993). For radio-loud AGNs (RLAGNs), additional, non-thermal X-ray emission is commonly associated with radio structures, lobes, and hot spots. This can generally be resolved from the nuclear X-ray emission with the high spatial resolution of *Chandra* (Wilkes et al. 2012; Worrall 2009; Harris & Krawczynski 2006). In the nucleus, the presence of an additional beamed, radio-jet-related component is demonstrated by the, on average, ~3× higher soft X-ray luminosity (Zamorani et al. 1981) and harder spectrum (Wilkes & Elvis 1987; Worrall & Wilkes 1990) of core-dominated (face-on), broad-lined RLAGNs in comparison with RQAGNs as observed with the *Einstein Observatory*.

The strong correlation between core radio and X-ray luminosities (Hardcastle & Worrall 1999; Worrall & Birkinshaw 1994; Fabbiano et al. 1984) supports a unification model in which beamed radio and X-ray emission originate at the base of the jet with the latter being related to the radio via synchrotron or synchrotron self-Compton processes. In lobe-dominated and edge-on sources, where a smaller beaming factor reduces the emission from this component, the X-ray emission lies above the X-ray/radio core correlation, and the spectrum is softer, consistent with a significant contribution from an accretion-related component as in RQAGNs (Hardcastle & Worrall 1999). At low redshift ($z < 1$), it has been possible to distinguish or place limits on the relative contributions from nuclear jet- and accretion-related X-ray components and confirm that the jet-related component is more strongly related to the core radio emission, and the absorption of the accretion-related component is related to source orientation (Hardcastle et al. 2009; Evans et al. 2006; Belsole et al. 2006). The lower signal-to-noise ratio (S/N) of the X-ray data for the higher redshift 3CRR sources presented here does not allow such separation.

1.2. Orientation, Obscuration, and Unification

While a level of unification of luminous quasars and radio galaxies is well established (Barthel 1989), the variations in the relative numbers of quasars and radio galaxies as a function of redshift and/or luminosity have called the simplest version of that scheme into question (Singal 1993; Lawrence & Elvis 1982). The ratio of obscured to all AGNs (the "obscured fraction") remains a matter of debate as different studies draw a variety of conclusions. At low redshift and luminosity, optical surveys show that type 2 AGNs appear to be more numerous than type 1 by a factor of approximately a few: obscured fractions of ~0.65–0.75 (Maiolino & Rieke 1995; Huchra & Burg 1992; Lawrence & Elvis 1982) are typical. Hard X-ray surveys, which are sensitive to gas rather than dust obscuration, find luminosity-dependent obscured fractions of 0.2–0.8 at low-redshift ($z \lesssim 0.1$; *INTEGRAL*, Sazonov et al. 2012; *Swift*/BAT, Burlon et al. 2011). High-luminosity, radio-selected samples indicate an obscured fraction of ~0.6 consistent with an unobscured half-opening angle of ~53° in unification models (Willott et al. 2000) but with a luminosity dependence (Grimes et al. 2005) that can be explained by the "receding torus model" (Falcke et al. 1995; Lawrence 1991). The 3CRR sample (Laing et al. 1983) also shows a dependence

on luminosity with obscured fractions of 0.67 in the redshift range $0.5 \lesssim z \lesssim 1$ (Barthel 1989) and 0.5 in the current sample ($1 \leqslant z \leqslant 2$). Estimates based on the luminosity of the narrow, optical [O III]λ5007 emission line show a range of 0.4–0.9, also decreasing with luminosity (Simpson 2005). X-ray surveys, again measuring the absorbing gas, generally conclude that the obscured fraction decreases with luminosity and increases with redshift, covering a range of ∼0.1–0.8 (Hasinger 2008; Treister & Urry 2006; La Franca et al. 2005), although the redshift dependence may only be present at high luminosities ($L_X > 10^{44}$ erg s^{-1}; Iwasawa et al. 2012; Gilli et al. 2010). However, Dwelly & Page (2006) find no relation between the obscured fraction and either luminosity or redshift in their analysis of deep *XMM-Newton* observations of the Chandra Deep Field South (CDFS). Estimates based on the IR emission imply a higher obscured fraction at high luminosity (∼0.3–0.6), a difference that may be due to missing highly obscured sources in the X-ray surveys (Polletta et al. 2008; Treister et al. 2008).

An alternate explanation for a luminosity dependence of the obscured fraction is contamination by a second population of sources at low luminosity which are not standard, actively accreting AGNs (Grimes et al. 2004; Willott et al. 2000). There is a significant subset of low-luminosity narrow-line radio galaxies (NLRGs) with low-ionization emission lines (low-ionization emission-line radio galaxy, LERG). Most FRI-type radio sources (Fanaroff & Riley 1974) and a subset of the lower radio power ($P_{178\,\mathrm{MHz}} < 10^{26.5}$ W Hz^{-1} sr^{-1}) FRII-type (Chiaberge et al. 2002; Grimes et al. 2004) are classified as LERGs. LERGs generally have weak, largely unobscured X-ray emission (Hardcastle et al. 2009) and weak mid-IR emission ($L(15\,\mu\mathrm{m}) < 8 \times 10^{43}$ erg s^{-1}; Ogle et al. 2006), both of which correlate with AGN luminosity indicators such as [O III] λ5007 emission-line luminosity (L[O III]; Dicken et al. 2009; Maiolino & Rieke 1995) and core radio strength. Thus, there is no evidence for a hidden, actively accreting nucleus, and LERGs may be powered by a radiatively inefficient accretion flow (Hardcastle et al. 2009; Evans et al. 2006; Ogle et al. 2006; Ghisellini & Celotti 2001). In this case, the unresolved radio, IR, and X-ray cores would be purely jet related rather than accretion related, e.g., as in M87 (Whysong & Antonucci 2004; Willott et al. 2000), and LERGs would not be part of the primary AGN population. The obscured fraction in the 3CRR sample determined without the LERGs is ∼0.5–0.6 with little/no dependence on redshift or luminosity (Ogle et al. 2006; Barthel 1989). It is clear that studies of the obscured fraction as a function of luminosity and z need to take into account source classification.

Spitzer studies of luminous 3CRR sources, i.e., excluding LERGs, from $0.05 < z < 2.0$ show no luminosity dependence of the obscured fraction, and thus support simple unification. At shorter wavelengths, our multi-wavelength study of the high-redshift ($z > 1$) 3CRR radio sample has demonstrated a marked difference between the *Spitzer*-observed IR SEDs of radio galaxies and quasars (Haas et al. 2008; Leipski et al. 2010; Ogle et al. 2006; Shi et al. 2005) which can be explained by nuclear obscuration of a randomly oriented sample in a unification model. Studies of lower-redshift 3CRs agree but also show evidence for a contribution to the inclination dependence from beamed emission (Cleary et al. 2007). At longer wavelengths, 24 μm and 70 μm, emission is unrelated to the source orientation (Dicken et al. 2009; Haas et al. 2004). *Herschel* observations suggest a significant contribution by star formation, expected to be independent of obscuration, in the far-IR for a subset of the sources (Barthel et al. 2012), supporting the results by Tadhunter et al. (2007). The inner parts of the narrow emission-line regions (NLR) may also be obscured, weakening the [O III] λ5007 emission line (Haas et al. 2005; Jackson & Browne 1990) but not [O II] λ3727 (Hes et al. 1993), and resulting in the higher-ionization lines being visible only in the IR. However, for the highest luminosity radio sources this seems not to be a large effect (Grimes et al. 2004; Jackson & Rawlings 1997), perhaps due to the more extended and so less obscured NLR in higher luminosity radio sources (Best et al. 2000).

1.3. This Paper

The high-redshift 3CRR sample, which includes only powerful, actively accreting AGNs (no LERGs) with a limited range of both luminosity and redshift, is a particularly uniform and well-suited sample with which to investigate the relation of the full SED to orientation/obscuration and to study the properties of the obscuring material. This paper describes the 3CRR sample (Section 2), presents our analysis of new and existing *Chandra* and *XMM-Newton* data (Section 3), characterizes the X-ray properties and investigates their relation to radio and IR emission (Section 4), discusses the results in the context of unification models (Section 5), and summarizes the conclusions (Section 6).

Throughout the paper, we assume a ΛCDM cosmology with $H_o = 71$ km s^{-1} Mpc^{-1}, $\Omega_M = 0.27$, and $\Omega_\Lambda = 0.73$ (Larson et al. 2011).

2. THE SAMPLE AND SUPPORTING DATA

The 3CRR catalog (Laing et al. 1983) contains 180 radio galaxies and quasi-stellar radio sources, quasars, up to redshift $z = 2.5$ and is 100% complete to a flux of 10 Jy at 178 MHz. At these low frequencies, all sources are dominated by emission from the radio lobes resulting in little/no bias based on the orientation of the source. The 3CRR sample has been studied in detail over many wavebands. The radio morphologies are well known and their radio sizes, lobe separations and jet prominence, and core fractions at higher frequencies (5 GHz) permit estimates of their radio axis orientation. We have selected a complete sample of high-redshift ($1 < z < 2$), and thus high-luminosity, 3CRR sources to ensure they are actively accreting, that none are LERGs (Hine & Longair 1979), and that the AGN dominates the bolometric luminosity of the source. The complete sample of 38 3CRR high-z sources[11] (Table 1) includes 21 lobe-dominated, steep spectrum quasars (a.k.a. broad-line radio galaxies, quasi-stellar objects (QSOs)) and 17 NLRGs, all of Fanaroff–Riley type FRII with double lobes of $P(178\,\mathrm{MHz}) > 10^{26.5}$ W Hz^{-1} generally extending far beyond the host galaxy. A subset of both types (six quasars, two NLRGs) has steep radio spectra ($\alpha > 0.5$) and compact (<10 kpc) structure (compact steep spectrum, CSS; O'Dea 1998; Fanti et al. 1985). There is at most one marginally core-dominated radio source, 3C 245,[12] in this sample so that beamed emission is not generally dominant.

Because of their brightness ($F(178\,\mathrm{MHz}) > 10$ Jy), the complete nature of the survey, the comprehensive multi-wavelength data available, and their high luminosity, the high-redshift 3CRR sources constitute an excellent sample with which to

[11] Which includes two 4C sources found by Laing et al. (1983) to match the 3CRR selection criteria.

[12] A compact triple source with a steep radio spectrum (Barthel et al. 1984; Foley & Barthel 1990) for which a variable core may result in a high core fraction.

Table 1
X-Ray Observations and Other Properties of the 3CRR High-redshift Sample

Name	ObsID	Date Obs. (UT)	R.A. (J2000.0)	Decl. (J2000)	z	Exp. Time (ks)	Source Type	Galactic N_H (10^{20}cm^{-2})	Ref. X-Ray	F(5 GHz) (Jy (tot))	log R_{CD}	log νL_R(5 GHz) (erg s^{-1} (tot))	Ref. Radio
3CRR 009	1595	2001 Jun 10	00:20:25.2	+15:40:55	2.009	19.88	QSO	4.16	1	0.546	−2.04	44.91	14
3CRR 013	9241	2008 Jun 01	00:34:14.5	+39:24:17	1.351	19.53	NLRG	6.39		0.397	−3.04	44.35	15
3CRR 014	9242	2008 May 29	00:36:06.5	+18:37:59	1.469	3.00	QSO	4.12		0.606	−1.75	44.62	16
3CRR 043	9324	2008 Jun 17	01:29:59.8	+23:38:20	1.459	3.04	QSO/CSS	7.13		1.082	<−1.22	44.87	17
3CRR 065	9243	2008 Jun 30	02:23:43.2	+40:00:52	1.176	20.91	NLRG	6.12		0.765	−3.17	44.48	15
3CRR 068.1	9244	2008 Feb 10	02:32:28.9	+34:23:47	1.238	3.05	QSO	6.02		0.824	−2.87	44.57	18
3CRR 068.2	9245	2008 Mar 06	02:34:23.8	+31:34:17	1.575	19.88	NLRG	7.78		0.179	−2.63	44.17	15
3CRR 181	9246	2009 Feb 12	07:28:10.3	+14:37:36	1.382	3.02	QSO	6.83		0.655	−2.03	44.59	19
3CRR 186	3098	2002 May 16	07:44:17.4	+37:53:17	1.067	34.44	QSO/CSS	5.64	2	0.377	−1.38	44.07	17
3CRR 190	9247	2007 Dec 31	08:01:33.5	+14:14:42	1.195	3.06	QSO/CSS	2.65		0.814	−1.01	44.53	17
3CRR 191	5626	2004 Dec 12	08:04:47.9	+10:15:23	1.956	19.77	QSO	2.44	3	0.457	−0.99	44.81	20
3CRR 204	9248	2008 Jan 13	08:37:44.9	+65:13:35	1.112	3.05	QSO	4.27		0.338	−1.06	44.07	14
3CRR 205	9249	2008 Jan 26	08:39:06.4	+57:54:17	1.534	96.72	QSO	4.51	5	0.665	−1.51	44.71	21
3CRR 208	9250	2008 Jan 8	08:53:08.8	+13:52:55	1.110	3.01	QSO	3.59		0.536	−0.98	44.26	14
3CRR 212	434	2000 Oct 26	08:58:41.5	+14:09:44	1.048	18.05	QSO	3.63	4	0.884	−0.69	44.42	22
3CRR 239	0306370701	2005 Apr 24	10:11:45.4	+46:28:20	1.781	14	NLRG	0.90	5	0.328	−2.82	44.56	15
3CRR 241	9251	2008 Mar 13	10:21:54.5	+21:59:30	1.617	18.93	NLRG/CSS	2.02	5	0.338	−2.05	44.47	23
3CRR 245	2136	2001 Feb 12	10:42:44.6	+12:03:31	1.029	10.40	QSO	2.87	3	1.38	+0.29	44.59	16
3CRR 252	9252	2008 Mar 11	11:11:33.0	+35:40:42	1.100	19.45	NLRG	1.73		0.318	−2.46	44.03	18
3CRR 266	9253	2008 Feb 16	11:45:43.4	+49:46:08	1.275	18.23	NLRG	1.80		0.318	<−3.27	44.19	15
3CRR 267	9254	2008 Jul 7	11:49:56.5	+12:47:19	1.140	19.18	NLRG	2.90		0.586	−2.29	44.33	15
3CRR 268.4	9325	2009 Feb 23	12:09:13.6	+43:39:21	1.398	3.02	QSO	1.30		0.596	−1.04	44.56	24
3CRR 270.1	9255	2008 Feb 16	12:20:33.9	+33:43:12	1.532	9.67	QSO	1.29	6	0.864	−0.55	44.82	16
3CRR 287	3103	2002 Jan 6	13:30:37.7	+25:09:11	1.055	39.93	QSO/CSS	1.08	2	3.237	...	44.99	25
3CRR 294	3207	2002 Feb 27	14:06:44.0	+34:11:25	1.779	123.63	NLRG	1.21	7	0.278	−2.72	44.49	24
3CRR 318	9256	2008 Apr 5	15:20:5.4	+20:16:06	1.574	9.78	QSO/CSS	4.01	5	0.745	<−0.86	44.79	26
3CRR 322	0028540301	2002 May 17	15:35:01.2	+55:36:53	1.681	10.0/6.5[12]	NLRG	1.34	8	0.457	−3.18	44.64	27
3CRR 324	326	2000 Jun 25	15:49:48.9	+21:25:38	1.206	42.15	NLRG	4.31	9	0.606	<−3.64	44.41	28
3CRR 325	4818	2005 Apr 17	15:49:58.4	+62:41:22	1.135	28.66	QSO	1.65	10	0.824	−2.53	44.48	18
3CRR 356	9257	2008 Jan 20	17:24:19.0	+50:57:40	1.079	19.87	NLRG	2.76		0.377	−2.53	44.08	29
4C 16.49	9262	2008 Jan 21	17:34:42.6	+16:00:31	1.880	3.0	QSO	6.64		0.320	−1.28	44.61	32
4C 13.66	9263	2008 Feb 5	18:01:38.9	+13:51:24	1.450	19.90	NLRG/CSS	11.15		0.340	<−2.23	44.36	31
3CRR 368	9258	2008 Jun 1	18:05:6.3	+11:01:33	1.131	19.90	NLRG	9.03		0.209	<−3.00	43.88	28
3CRR 432	5624	2005 Jan 7	21:22:46.2	+17:04:38	1.785	19.78	QSO	7.34	5,11	0.308	−1.60	44.54	14
3CRR 437	9259	2008 Jan 7	21:47:25.1	+15:20:37	1.480	19.88	NLRG	7.16		0.874	<−3.86	44.79	15
3CRR 454.0	0306370201	2005 May 25	22:51:34.7	+18:48:40	1.757	16	QSO/CSS	5.90	5	0.784	<−0.47	44.93	17
3CRR 469.1	9260	2009 May 18	23:55:23.3	+79:55:20	1.336	20.18	NLRG	13.74	13	0.407	−2.19	44.35	30
3CRR 470	9261	2008 Mar 3	23:58:35.3	+44:04:39	1.653	19.91	NLRG	9.46		0.546	−2.43	44.70	15

References. (1) Fabian et al. 2003a; (2) Siemiginowska et al. 2008; (3) Gambill et al. 2003; (4) Aldcroft et al. 2003; (5) Salvati et al. (2008) (*XMM-Newton* data); (6) Wilkes et al. 2012; (7) Fabian et al. 2001, 2003b; (8) Belsole et al. (2004) (*XMM-Newton* data, extended emission only); (9) Hardcastle et al. 2004; (10) Hardcastle et al. (2009) (used earlier, incorrect redshift of 0.86); (11) Erlund et al. 2006; (12) *XMM-Newton* exposures in MOS/pn, after screening for periods of high background; (13) Laskar et al. (2010) (*XMM-Newton* data); (14) Bridle et al. 1994; (15) Best et al. 1997; (16) Akujor et al. 1994; (17) Ludke et al. 1998; (18) Fernini et al. 1997; (19) Mantovani et al. 1992; (20) Akujor & Garrington 1995; (21) Lonsdale & Barthel 1984; (22) Akujor et al. 1991; (23) Fanti et al. 1985; (24) Liu et al. 1992; (25) Fanti et al. 1989; (26) Spencer et al. 1991; (27) Law-Green et al. 1995; (28) Best et al. 1998; (29) Fernini et al. 1993; (30) Longair 1975; (31) Rawlings et al. 1996; (32) Lonsdale et al. 1993.

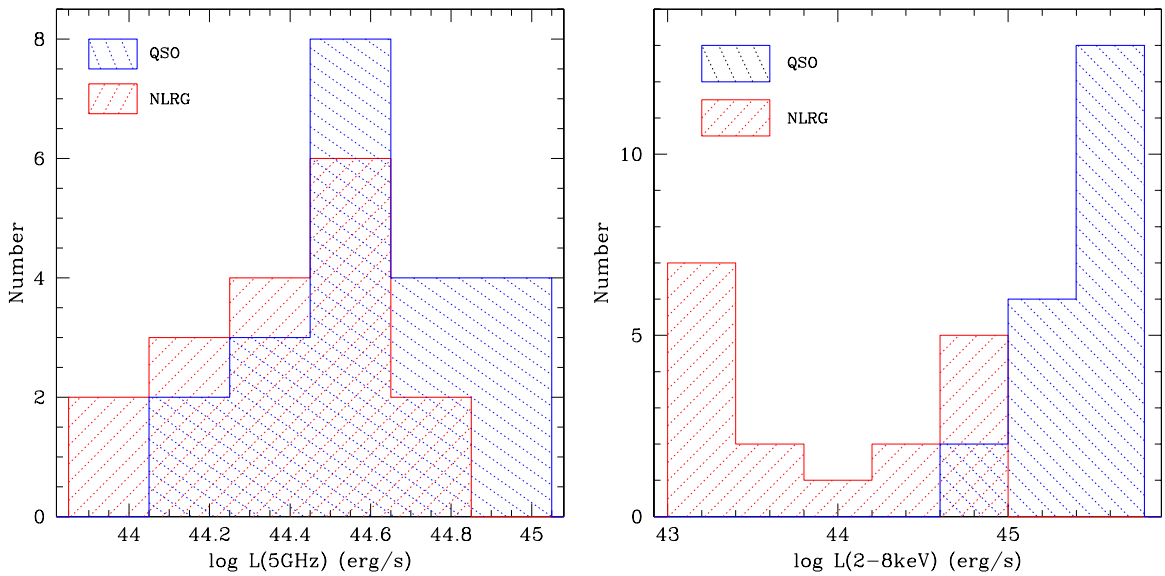

Figure 1. Comparison of the distributions of total rest-frame 5 GHz radio (left) and hard-band, nuclear X-ray (right) luminosities, uncorrected for intrinsic absorption, for the quasars (QSOs, blue) and NLRGs (red). In the radio, the range is small (within 1 dex) with a small shift to higher luminosities for the quasars indicating a ∼30% contribution from the beamed core at this relatively high frequency. In the X-rays, the full distribution covers ∼2.5 dex and the quasars are easily distinguishable by their brighter X-ray emission.

(A color version of this figure is available in the online journal.)

study orientation-based effects. The mean 5 GHz luminosity ($\log \nu\ L_{\rm R}(5\,{\rm GHz}) \sim 44.5$ erg s^{-1}; Figure 1 (left)) is about five times higher than for the 3CRR sources at $0.5 < z < 1$. The high redshift lowers the effects of X-ray absorption, which largely shifts out of the *Chandra* band unless the source is close to CT. This strong negative k correction means that the X-ray flux of heavily absorbed AGNs is not such a strong function of redshift in this range (Wilman & Fabian 1999), and CT AGNs are detectable. *Spitzer* IRAC and MIPS photometry have been obtained to delineate the IR continuum for the full sample and IRS spectroscopy for those in the range $1.0 < z < 1.4$ (Haas et al. 2008; Leipski et al. 2010).

3. X-RAY DATA AND ANALYSIS

Eleven sources in our high-z 3CRR sample, two NLRGs and nine quasars, were previously observed by *Chandra*, and four sources, three NLRGs (one in common with *Chandra*) and one quasar, with *XMM-Newton*. New *Chandra* ACIS-S observations were obtained for the remaining 24 quasars and NLRGs and for 3C 270.1 where the existing *Chandra* data were of poor quality. The exposure times were set for a detection at expected levels for NLRGs and quasars as a function of redshift. Sub-arrays were used for the brightest quasars to avoid pileup issues. The observations used in this paper, both new and archival, are listed in Table 1 along with known properties of the sources and references to published analysis of existing *Chandra* and/or *XMM-Newton* X-ray data. All but one sources were detected making this the most complete X-ray-observed sample of AGNs to date. There is a wide range of S/N from a few counts for the faintest NLRG to ∼1000 net counts for the brightest quasars.

The *Chandra* data were processed using the standard pipeline with calibration products appropriate for their observation dates. Archived *Chandra* data sets observed in ACIS VFAINT mode were reprocessed to take advantage of improved calibration of the CTI correction and background cleaning. Counts were extracted from a 2″.2 radius circle (to enclose the full point-spread function) centered on the X-ray source position for energy bands: broad (B, 0.3–8.0 keV), soft (S, 0.3–2.0 keV), and hard (H, 2.0–8.0 keV). Background counts were extracted in the same energy bands from an annulus centered on the position of each source with inner and outer radii of 15″ and 35″, respectively, adjusted if necessary to exclude nearby sources. Any sources remaining within the background annulus were removed. The resulting net counts and hardness ratios[13] are given in Table 2.

In order to provide a uniform set of derived X-ray properties, all *Chandra*-observed sources were run through an automated spectral analysis process using the Levenberg–Marquardt optimization method in CIAO/Sherpa with the χ^2 statistic including the Gehrels variance function, which allows for a Poisson distribution for low-count sources. Two spectral fits were performed: the first fit assumed a power-law spectrum with a canonical slope $\Gamma = 1.9$ (Just et al. 2007; Mushotzky et al. 1993) and Galactic absorption as characterized by the equivalent hydrogen column density ($N_{\rm H}$(gal), Table 1; Dickey & Lockman 1990), and the second added an intrinsic absorption component at the redshift of the source ($N_{\rm H}$(int)). The results were inspected individually, and those for the best spectral fits are listed in Table 2, including Galactic and intrinsic absorption-corrected fluxes and luminosities in standard bands. When no significant $N_{\rm H}$(int) was detected, a 3σ upper limit is listed. Spectral fits for sources with low net counts (<50) provided no useful constraint on $N_{\rm H}$(int). For sources where the data have sufficient net counts (>700), mostly quasars, the results of a third spectral fit allowing the power-law slope to be free are also listed in Table 2. Derived spectral parameters are consistent with those reported in published data except where noted in the table. Detected $N_{\rm H}$(int), indicating absorption in excess of the Galactic column density, is most likely to be absorption intrinsic to the quasar associated with the nucleus and/or the host galaxy. Although unlikely, a

[13] Hardness ratio based on the counts, HR $= (H - S)/(H + S)$ with uncertainties determined using the Bayesian estimation (BEHR) method (Park et al. 2006).

Table 2
X-Ray Source Parameters[a]

Name	Type[b]	Net Counts (0.3–8 keV)	Background Counts (0.3–8 keV)	χ^2	Γ	$N_{\rm H}$(int) (10^{22} cm^{-2})	f(1 keV)[c] (10^{-6})	F(0.3–8 keV)[c] (10^{-14})	log L(0.3–8 keV)[d] (erg s^{-1})	HR[e] $\frac{(H-S)}{(H+S)}$
3C 009	Q	805.8 ± 28.4	1.19 ± 0.08	0.9	1.9	<0.45	$47.5^{+2.9}_{-2.8}$	26.2 ± 0.9	$45.85^{+0.01}_{-0.02}$	$-0.53^{+0.1}_{-0.1}$
				0.8	1.74 ± 0.08	<0.28	$44.9^{+2.2}_{-2.5}$	27.4 ± 1.6		
3C 013	N/CT	15.3 ± 4.0	0.68 ± 0.06	0.3	1.9	...	$0.8^{+0.5}_{-0.5}$	0.4 ± 0.2	$43.6^{+0.2}_{-0.4}$	$-0.51^{+0.2}_{-0.2}$
3C 014	Q	238.9 ± 15.5	0.14 ± 0.03	0.6	1.9	$0.7^{+0.4}_{-0.3}$	$131.8^{+16.0}_{-14.9}$	73.0 ± 3.9	$45.97^{+0.03}_{-0.02}$	$-0.38^{+0.1}_{-0.1}$
3C 043	Q/C	170.8 ± 13.1	0.16 ± 0.03	0.5	1.9	<1.5	$86.6^{+13.4}_{-12.0}$	47.7 ± 3.2	$45.77^{+0.03}_{-0.03}$	$-0.40^{+0.1}_{-0.1}$
3C 065	N	205.2 ± 14.4	0.81 ± 0.06	0.6	1.9	$9.3^{+2.2}_{-1.8}$	$45.4^{+7.6}_{-7.1}$	25.1 ± 0.3	$45.26^{+0.01}_{-0.01}$	$+0.23^{+0.1}_{-0.1}$
3C 068.1	Q	43.7 ± 6.6	0.29 ± 0.04	0.4	1.9	$9.0^{+7.3}_{-4.6}$	$57.4^{+28.9}_{-23.6}$	131.8 ± 1.6	$45.42^{+0.02}_{-0.02}$	$+0.13^{+0.1}_{-0.2}$
3C 068.2	N/CT	8.2 ± 3.0	0.77 ± 0.06	0.2	1.9	...	$0.37^{+0.35}_{-0.35}$	0.21 ± 0.16	$43.5^{+0.2}_{-0.6}$	$+0.33^{+0.4}_{-0.3}$
3C 181	Q	188.8 ± 13.8	0.16 ± 0.03	0.7	1.9	<0.6	$86.1^{+10.4}_{-8.3}$	47.3 ± 4.2	$45.71^{+0.04}_{-0.04}$	$-0.53^{+0.1}_{-0.1}$
3C 186[f]	Q/C	1984.4 ± 44.6	4.65 ± 0.15	1.3	1.9	<0.01	$70.5^{+3.5}_{-3.2}$	39.0 ± 1.0	$45.35^{+0.01}_{-0.01}$	$-0.63^{+0.02}_{-0.02}$
				1.2	2.1 ± 0.1	<0.03	$72.9^{+3.6}_{-1.9}$	36.8 ± 1.0		
3C 190	Q/C	172.8 ± 13.2	0.16 ± 0.03	0.9	1.9	$0.4^{+0.3}_{-0.2}$	$80.5^{+11.7}_{-11.0}$	45.2 ± 3.6	$45.54^{+0.03}_{-0.04}$	$-0.52^{+0.1}_{-0.1}$
3C 191	Q	824.2 ± 28.7	0.76 ± 0.06	0.8	1.9	<0.45	$51.4^{+3.1}_{-3.0}$	28.4 ± 1.1	$45.86^{+0.01}_{-0.02}$	$-0.52^{+0.03}_{-0.03}$
				0.7	1.70 ± 0.08	<0.25	$47.5^{+3.1}_{-2.1}$	29.6 ± 1.9		
3C 204	Q	358.8 ± 19.0	0.20 ± 0.03	0.6	1.9	<0.4	$168.9^{+14.4}_{-14.0}$	92.6 ± 5.2	$45.86^{+0.01}_{-0.02}$	$-0.57^{+0.1}_{-0.1}$
3C 205[g]	Q	1006.5 ± 31.7	0.51 ± 0.05	1.0	1.9	$0.42^{+0.16}_{-0.14}$	$164.4^{+8.8}_{-8.6}$	90.8 ± 2.5	$46.11^{+0.01}_{-0.02}$	$-0.43^{+0.1}_{-0.1}$
				0.6	$1.60^{+0.08}_{-0.05}$	<0.4	$134.5^{+10.0}_{-5.3}$	91.4 ± 4.8		
3C 208	Q	280.8 ± 16.8	0.20 ± 0.03	0.8	1.9	<0.5	$126.6^{+14.9}_{-10.0}$	69.6 ± 5.0	$45.65^{+0.03}_{-0.04}$	$-0.47^{+0.1}_{-0.1}$
3C 212	Q	3944.1 ± 62.8	0.92 ± 0.07	0.8	1.9	$0.46^{+0.03}_{-0.03}$	$330.2^{+8.2}_{-8.1}$	182.5 ± 1.9	$46.00^{+0.01}_{-0.01}$	$-0.49^{+0.01}_{-0.01}$
				0.6	1.68 ± 0.04	$0.32^{+0.04}_{-0.03}$	$290.8^{+10.7}_{-10.3}$	183.5 ± 3.4		
3C 239[h]	N	...	...	...	...	...	...	...	$44.69^{+0.06}_{-0.06}$	-0.7
3C 241	N/C	147.2 ± 12.2	0.76 ± 0.06	0.7	1.9	$6.2^{+2.4}_{-1.7}$	$22.7^{+4.6}_{-4.0}$	12.6 ± 0.4	$45.30^{+0.01}_{-0.01}$	$-0.05^{+0.1}_{-0.1}$
3C 245	Q	2067.4 ± 45.5	0.65 ± 0.07	1.4	1.4	<0.09	$236.0^{+8.6}_{-8.4}$	130.3 ± 2.6	$45.84^{+0.01}_{-0.01}$	$-0.57^{+0.1}_{-0.1}$
				1.0	$1.65^{+0.05}_{-0.04}$	<0.02	$218.6^{+8.2}_{-4.4}$	141.4 ± 5.8		
3C 252	N	89.6 ± 9.5	1.45 ± 0.09	1.1	1.9	$10.5^{+7.5}_{-3.9}$	$21.5^{+9.8}_{-6.4}$	11.9 ± 0.2	$44.87^{+0.01}_{-0.01}$	$+0.43^{+0.1}_{-0.1}$
3C 266	N/CT	19.2 ± 4.5	0.77 ± 0.06	0.3	1.9	...	$0.71^{+0.44}_{-0.44}$	0.36 ± 0.23	$43.51^{+0.21}_{-0.44}$	$+0.19^{+0.2}_{-0.2}$
3C 267	N	167.2 ± 13.0	0.82 ± 0.06	1.3	1.9	$10.8^{+3.7}_{-2.6}$	$39.8^{+9.5}_{-7.8}$	22.0 ± 0.4	$45.18^{+0.01}_{-0.01}$	$+0.31^{+0.1}_{-0.1}$
3C 268.4	Q	291.8 ± 17.1	0.18 ± 0.03	1.2	1.9	$0.4^{+0.3}_{-0.2}$	$142.7^{+15.8}_{-14.7}$	78.6 ± 5.0	$45.94^{+0.03}_{-0.02}$	$-0.40^{+0.1}_{-0.1}$
3C 270.1	Q	734.6 ± 27.1	0.45 ± 0.05	1.2	1.9	<0.36	$95.5^{+4.6}_{-4.6}$	53.2 ± 2.5	$45.87^{+0.02}_{-0.02}$	$-0.53^{+0.1}_{-0.1}$
				1.1	1.69 ± 0.08	<0.24	$91.2^{+6.1}_{-4.3}$	57.6 ± 4.3		
3C 287	Q/C	3862.0 ± 62.2	2.01 ± 0.14	0.6	1.9	<0.06	$120.0^{+2.9}_{-2.9}$	66.3 ± 1.2	$45.57^{+0.01}_{-0.01}$	$-0.63^{+0.01}_{-0.01}$
				0.6	$1.82^{-0.04}_{+0.05}$	<0.09	$115.3^{+4.0}_{-3.2}$	66.6 ± 1.7		
3C 294[i]	N/CT	202.9 ± 14.4	3.08 ± 0.13	3.6	1.9	...	0.61	0.34 ± 0.06	$43.83^{+0.08}_{-0.08}$	$+0.52^{+0.06}_{-0.06}$
3C 318	Q/C	267.5 ± 16.4	0.50 ± 0.05	0.5	1.9	<0.8	$38.8^{+4.2}_{-3.5}$	21.4 ± 1.6	$45.50^{+0.04}_{-0.03}$	$-0.50^{+0.1}_{-0.1}$
3C 322[j]	N	17.6 ± 6.5	12.4 ± 3.5	...	...	...	...	<1.5	<44.44	...
3C 324[k]	N/CT	45.2 ± 6.9	2.80 ± 0.12	0.4	1.9	...	$0.9^{+0.2}_{-0.2}$	0.49 ± 0.11	$43.58^{+0.09}_{-0.11}$	$-0.28^{+0.16}_{-0.13}$
3C 325	Q	360.1 ± 19.0	0.92 ± 0.07	0.8	1.9	$6.2^{+1.0}_{-0.9}$	$44.7^{+5.2}_{-4.9}$	24.6 ± 0.3	$45.22^{+0.01}_{-0.01}$	$+0.05^{+0.06}_{-0.05}$
3C 356	N/CT	26.1 ± 5.2	0.87 ± 0.07	0.5	1.9	...	$0.9^{+0.4}_{-0.4}$	0.52 ± 0.24	$43.49^{+0.17}_{-0.27}$	$+0.33^{+0.2}_{-0.2}$
4C 16.49	Q	183.8 ± 13.6	0.22 ± 0.03	0.7	1.9	<0.5	$83.7^{+11.7}_{-6.8}$	46.9 ± 4.0	$46.03^{+0.04}_{-0.04}$	$-0.54^{+0.1}_{-0.1}$
4C 13.66	N/C/CT	20.0 ± 4.6	0.98 ± 0.07	0.7	1.9	...	$1.2^{+0.6}_{-0.6}$	0.61 ± 0.23	$43.87^{+0.14}_{-0.20}$	$-0.54^{+0.2}_{-0.2}$
3C 368[k]	N/CT	17.1 ± 4.2	0.86 ± 0.07	0.1	1.9	...	$1.0^{+0.6}_{-0.6}$	0.53 ± 0.24	$43.55^{+0.16}_{-0.26}$	$-0.34^{+0.2}_{-0.3}$
3C 432	Q	771.2 ± 27.8	0.76 ± 0.06	0.8	1.9	<0.6	$55.6^{+3.5}_{-3.4}$	30.7 ± 0.9	$45.79^{+0.02}_{-0.01}$	$-0.50^{+0.03}_{-0.03}$
				0.8	$1.74^{+0.11}_{-0.07}$	<0.67	$50.3^{+4.9}_{-2.5}$	30.6 ± 1.7		
3C 437	N/CT	9.8 ± 3.3	0.84 ± 0.06	0.4	1.9	...	$0.38^{+0.35}_{-0.35}$	0.19 ± 0.17	$43.39^{+0.28}_{-0.98}$	$+0.28^{+0.3}_{-0.3}$
3C 454.0[h]	Q/C	...	...	...	...	<0.13	...	...	$45.70^{+0.03}_{-0.03}$	-0.3
3C 469.1	N	80.9 ± 9.1	1.12 ± 0.08	0.3	1.9	$26.9^{+14.8}_{-8.9}$	$32.6^{+14.3}_{-10.1}$	18.0 ± 0.2	$45.26^{+0.01}_{-0.01}$	$+0.61^{+0.1}_{-0.1}$
3C 470	N	55.2 ± 7.5	0.85 ± 0.07	0.2	1.9	$50.7^{+22.8}_{-15.5}$	$29.1^{+13.2}_{-10.4}$	16.0 ± 0.2	$45.43^{+0.01}_{-0.01}$	$+0.74^{+0.1}_{-0.1}$

Notes.

[a] X-ray data were fit with a power law ($\Gamma = 1.9$) + Galactic absorption, plus intrinsic equivalent hydrogen column density ($N_{\rm H}$(int)). Generally, no constraints could be placed on $N_{\rm H}$(int) when the net counts were <50.

[b] Source Classification: Q, quasar; N, narrow line radio galaxy (NLRG); C, compact steep spectrum (CSS) source; CT, Compton thick candidate.

[c] Flux densities (in units of photons cm^{-2} s^{-1} keV^{-1}) and fluxes (in units of erg cm^{-2} s^{-1}) are quoted with 1σ errors and based on the best fit spectral model. Fits to all NLRGs with $\gtrsim$50 counts required intrinsic ($N_{\rm H}$(int)) absorption. Upper limits to $N_{\rm H}$(int) are quoted at 3σ.

[d] L(0.3–8 keV) is determined in the rest frame including a correction for any significant $N_{\rm H}$(int).

[e] Hardness ratios are calculated using BEHR (Park et al. 2006).

[f] Detailed spectral fits for this source and its surrounding cluster are presented in Siemiginowska et al. (2005, 2010).

[g] The X-ray spectrum is flat, $\Gamma \sim 1.6$, which results in an apparent $N_{\rm H}$(int) for the $\Gamma = 1.9$ fit.

[h] Equivalent *Chandra* luminosity and HR were derived based on published *XMM-Newton* spectral fits which reported no counts or flux (Salvati et al. 2008; Siemiginowska et al. 2010).

[i] A single power law does not provide a good fit to the data. A detailed spectral fit (Fabian et al. 2003b) yields $N_{\rm H} = 8.4^{+1.1}_{-0.9} \times 10^{23}$ cm^{-2}, dominated by a reflection component. This source is not included as a CT candidate in Section 5.1.

[j] The upper limit was determined directly from the *XMM-Newton* data set using an on-source circle of radius 8″. Due to the weak detection of extended emission aligned with the lobes, the counts are treated as an upper limit to any true core emission.

[k] Hardness ratios are significantly different using a smaller circle (1″ radius): 3C 324: $0.13^{+0.16}_{-0.20}$; 3C 368: $-0.01^{+0.35}_{-0.25}$.

contribution from absorption by intervening material/sources along the line of sight cannot be ruled out.

There are three sources with only *XMM-Newton* data: 3C 239/322/454.0. The results of published spectral analysis were used to derive equivalent *Chandra* quantities for 3C 239/454.0 (Salvati et al. 2008). For 3C 322 the *XMM-Newton* data showed no detection of the AGN (Belsole et al. 2004). In order to determine an upper limit, the data were measured directly (Tables 1 and 2).

About half the sample show significant extended X-ray emission. An example is 3C 270.1 (Wilkes et al. 2012) with X-ray emission related to the radio structure, as is often observed (Harris & Krawczynski 2006; Worrall 2009), along with possible detection of thermal emission from a surrounding cluster. The study of the extended X-ray emission will be covered in a later paper. Extranuclear emission originating close to the nucleus will generally not be resolved at these high redshifts. In cases with visible extent which may be contaminating the nuclear X-ray counts determined via the standard extraction region, an additional, smaller region was also used to better isolate the emission from the nucleus. When the results differ, a second set of hardness ratios is reported in Table 2, footnote k. These numbers were not used in our general analysis in order to ensure uniform measurements across the full sample.

4. RESULTS

4.1. X-Ray Luminosity

Since they are low-frequency (178 MHz) radio selected, for which the emission is generally optically thin, the quasars and NLRGs are well matched in this orientation-independent parameter. Figure 1 (left) shows the distributions of the total radio luminosity at the higher frequency of 5 GHz, where beaming is more important. The overlap remains good, with a small shift toward brighter luminosities for the quasars. The difference between the median luminosities of the NLRGs (log $L_{\rm R}(5\,{\rm GHz}) = 44.41$) and the quasars (log $L_{\rm R}(5\,{\rm GHz}) = 44.59$) indicates that beamed emission from the core contributes on average ∼30% of the radio luminosity in the lobe-dominated quasars and likely a similar fraction of the X-ray luminosity as well.

The distribution of X-ray luminosities derived from the initial power-law spectral fits, with no $N_{\rm H}$(int) included, is shown in Figure 1 (right). In contrast to the radio luminosity, the X-ray luminosity distributions barely overlap, demonstrating the well-known difference between the observed X-ray emission from quasars and NLRGs with the quasars factors of ∼10–1000 brighter (Hardcastle & Worrall 1999; Worrall et al. 1994). In this sample, the ratio of the median $L_{\rm X}$ for quasars and NLRGs is ∼100. Unification models interpret this difference as due to obscuration in the edge-on NLRGs.

4.2. X-Ray Hardness Ratio and Absorption

X-ray hardness ratio is an indicator of the intrinsic spectrum that can be used over a wide range of S/N. Assuming the primary power law dominates and that its spectral index is similar in all sources, the hardness ratio statistically indicates the amount of obscuration. Figure 2 shows a comparison of the distribution of X-ray hardness ratios determined using our standard X-ray analysis (Table 2) for the quasars and NLRGs in the 3CRR high-redshift sample. The quasars, with only two exceptions, show soft spectra covering a narrow range of hardness ratio (∼ −0.5),

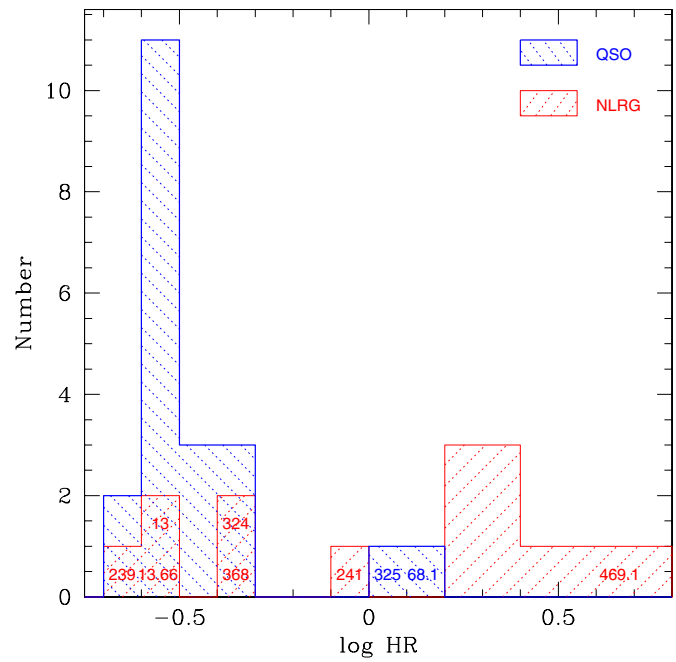

Figure 2. Histograms of the X-ray hardness ratios for quasars (QSOs, blue) and NLRGs (red) showing soft emission for all but two of the quasars and a wide range of hardness ratio for the NLRGs.

(A color version of this figure is available in the online journal.)

consistent with the average spectrum of a quasar: $\Gamma \sim 1.9$ and little/no obscuration. The NLRGs, on the other hand, cover a wide range of hardness ratios ($-0.7 < {\rm HR} < 0.7$). Five are consistent with the soft spectra of quasars, but the majority are significantly harder. The two harder quasars noted above 3C 68.1/325, along with NLRG 3C 241, lie between the quasars and NLRGs, having moderately hard spectra consistent with obscuration by material with $N_{\rm H}$(int) $\sim 10^{22}$–10^{23} cm^{-2}.

The X-ray spectra of quasars are known to include several components, limiting the accuracy with which any intrinsic obscuration can be determined in low S/N data (Section 1). For example, the presence of a soft excess or scattered nuclear emission decreases the estimated obscuration if not accounted for in the fits. By contrast, the presence of a reflection component would harden the effective X-ray slope at high energies, resulting in an overestimate of the obscuration in our single power-law fits to individual sources. Thus, both hardness ratios and single power-law spectral fits can be misleading in individual cases (Wilkes et al. 2005; Pounds et al. 2005). Higher S/N data than are available for the NLRGs in this sample are required to reliably de-convolve any multiple spectral and/or spatial components.

The $N_{\rm H}$(int) obtained from the spectral fits is shown in Figure 3 as a function of the observed hardness ratio with lines showing the relationship between $N_{\rm H}$(int) and HR for a single, absorbed power law with several slopes and redshifts superposed for comparison. The NLRGs trend similarly to models with the canonical quasar X-ray spectrum $\Gamma = 1.9$ (Just et al. 2007) with HRs indicating a maximum detected column density $\sim 7 \times 10^{23}$ cm^{-2}. The fitted spectral slopes for the seven quasars (non-CSS) with >700 net counts (Table 2) show a mean of 1.69 ± 0.05 and no evidence for a soft excess. This is harder than the standard slope of 1.9, consistent with a contribution from beamed, jet-related emission which generally has a harder ($\Gamma \sim 1.5$) slope (Wilkes & Elvis 1987, see Section 1.1).

Figure 4 shows the hardness ratio as a function of the broad band X-ray luminosity determined from the spectral fit in our

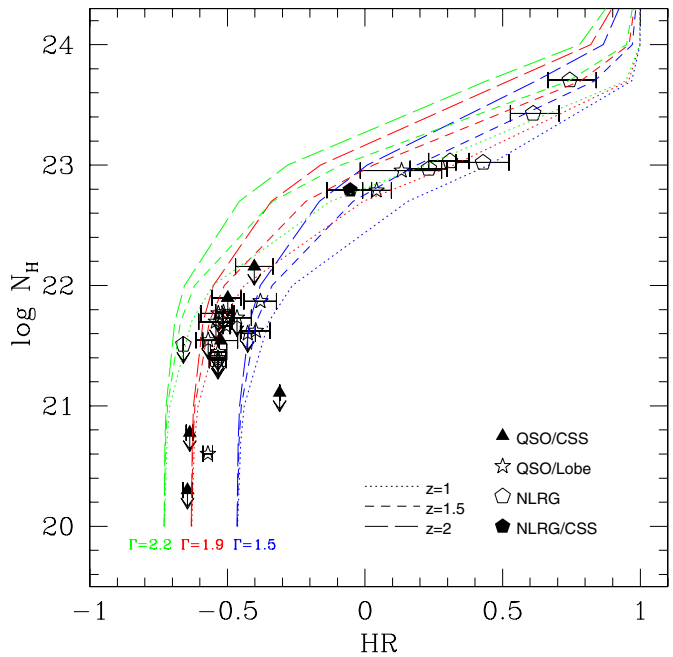

Figure 3. Fitted N_H(int) (when available) as a function of the observed hardness ratio. For comparison, the relationship between N_H(int) and HR for an absorbed power law is shown, assuming $\Gamma = 1.5$ (blue), 1.9 (red), 2.2 (green), at redshifts 1, 1.5, 2, ranges which cover the present sample. The different symbols indicate the class of source as shown in the legend.

(A color version of this figure is available in the online journal.)

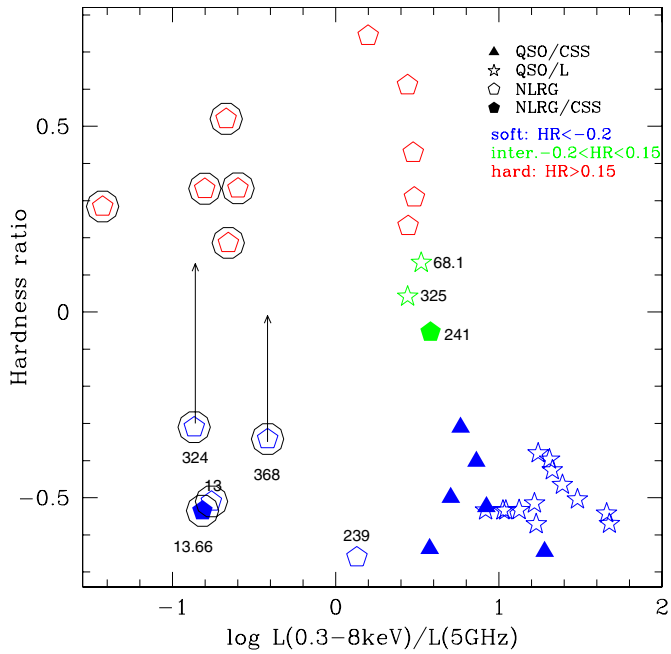

Figure 5. X-ray hardness ratio (HR) as a function of X-ray to total 5 GHz radio luminosity ratio, L_X/L_R. The symbol shapes and colors are indicated in the legend. The upward arrows for two soft NLRGs indicate the HR using a smaller (1″) extraction circle to exclude visible extended X-ray emission (Table 2, note k).

(A color version of this figure is available in the online journal.)

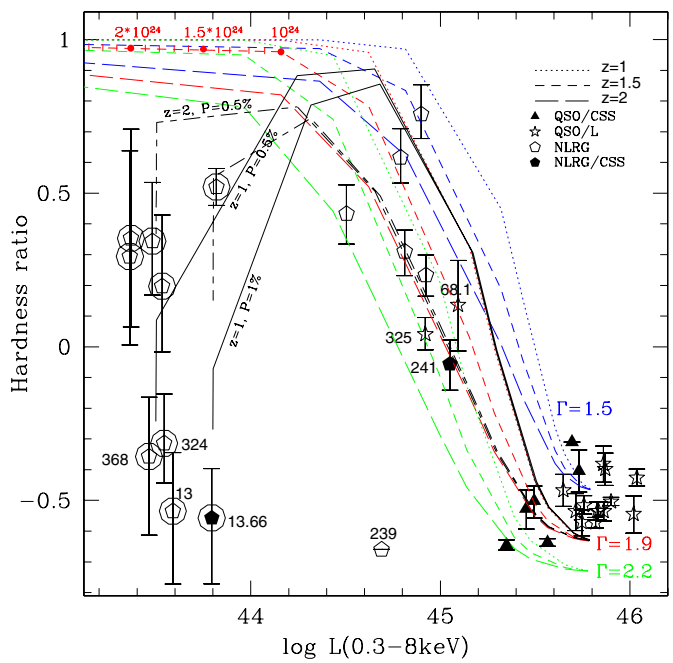

Figure 4. X-ray hardness ratio as a function of broad band (0.3–8 keV) X-ray luminosity in comparison with absorbed power-law models assuming $\Gamma = 1.5$ (blue), 1.9 (red), 2.2 (green), at redshifts 1, 1.5, 2 (dotted, short-dashed, and long-dashed lines, respectively), and covering $N_H(\text{int}) = 1 \times 10^{20}$ to 1×10^{25} cm^{-2}. L_X is determined without correcting for N_H(int) so as to demonstrate the effect of absorption on the deduced L_X. The large circles indicate sources with <50 counts, for which N_H(int) could not be constrained by the spectral fits. The red dots on the $\Gamma = 1.9$, $z = 1.5$ model curve (red short-dashed line) indicate N_H(int) of $(1, 1.5, 2) \times 10^{24}$ cm^{-2}. The black lines show the addition of an unabsorbed power law ($\Gamma = 1.9$) scattered at the 0.5% and 1% levels to the $z = 1, 2$ models (solid and dashed black lines, respectively), illustrating one possible explanation for the softer spectra in the X-ray weakest sources.

(A color version of this figure is available in the online journal.)

standard analysis but uncorrected for any deduced N_H(int). Models for a power-law X-ray spectrum for a luminosity typical of the quasars in the sample with a range of slope (Γ), intrinsic absorption (N_H(int)), and redshift are shown for comparison. The observed quantities are consistent with the models for X-ray luminosities above $\sim 4 \times 10^{44}$ erg cm^{-2} s^{-1}, where sources with lower luminosities than the quasars have harder HR as expected for mild absorption. However, as the luminosity decreases further, the observed hardness ratios remain constant or soften. This trend can be explained in terms of spectral complexity, where contributions from weaker components (e.g., soft excess, reflection) become significant as the dominant power-law emission is absorbed away. To illustrate the effect of a weaker component, the black lines in Figure 4 show the addition of nuclear power-law emission ($\Gamma = 1.9$) scattered from extended material at levels of 0.5% and 1% for $z = 1, 2$. This example demonstrates that an additional, soft component can explain the HRs of the lowest L_X NLRGs in this figure.

A more general measure of the relative X-ray luminosity is given by normalizing to the total radio luminosity. Figure 5 shows the hardness ratio as a function of X-ray to total radio luminosity ratio, L_X/L_R ($= L_X$ (0.3–8 keV)$/L_R$(5 GHz)). Since the range of L_X for the quasars is small, the trends are very similar to those in Figure 4. This figure clearly shows the three intermediate sources discussed earlier (quasars 3C 68.1/325 and NLRG 3C 241) which lie in between the rest of the quasars and NLRGs suggesting intermediate obscuration levels. The upward arrows indicate the change in HR for soft NLRGs 3C 324/368 when using a smaller (1″) circle to extract the counts, excluding some of the extended emission clearly present in these two sources (Table 2, footnote k).

For sources with <50 counts, the spectral fits do not provide useful constraints on N_H(int). However, based on the comparison between models and data in Figure 4, we conclude that

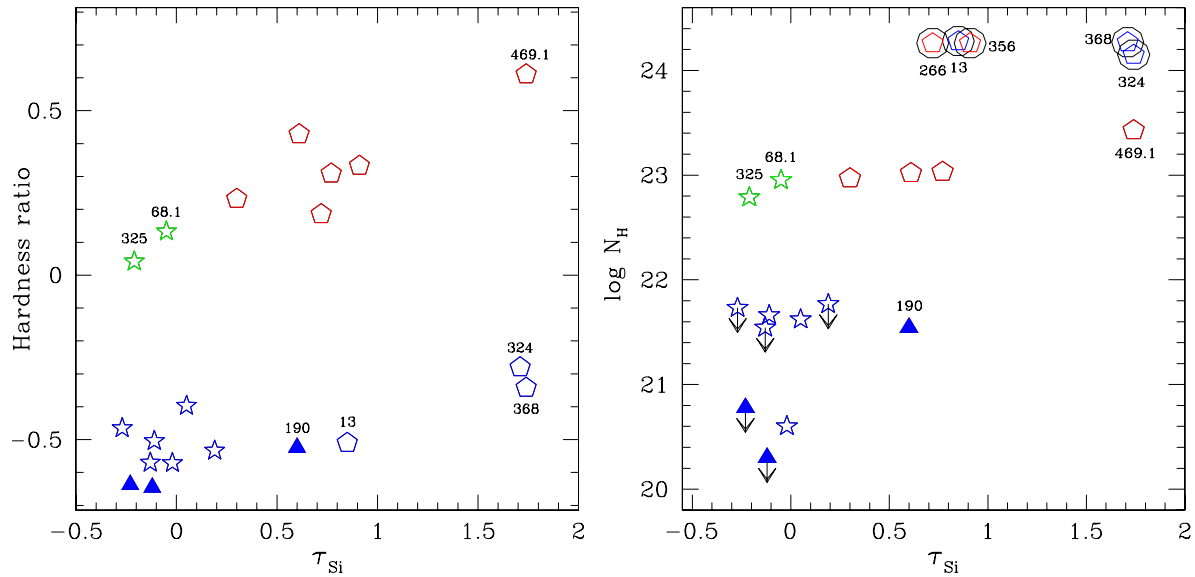

Figure 6. X-ray hardness ratio (HR, left) and the equivalent intrinsic hydrogren column density (N_H(int), right) estimated from spectral fits or L_X (circled data points) as a function of the *Spitzer*-measured optical depth of the silicate $\lambda 9.7\,\mu$m absorption $\tau_{9.7\,\mu m}$ (Leipski et al. 2010). The colors and symbols are as in Figure 5.

(A color version of this figure is available in the online journal.)

Table 3
N_H(int) for Low-count Sources Estimated from Figure 4

Name	N_H(int)[a] (10^{24} cm^{-2})
3C 13	1.8
3C 68.2	2.0
3C 266	1.8
3C 294	1.4
3C 324	1.8
3C 356	1.9
3C 368	1.9
3C 437	2.0
4C 13.66	1.4

Note. [a] Uncertainty is ±0.2, accounting for $1 < z < 2$, $1.5 < \Gamma < 2.2$.

the lower values of L_X and L_X/L_R in NLRGs are due to obscuration. Thus, L_X/L_R is a more reliable obscuration indicator than the X-ray HR which includes additional, soft X-ray emission components. The factor of ∼3–200× lower X-ray luminosities for the NLRGs indicate intrinsic column densities $N_H(\text{int}) \sim 5 \times 10^{22}$ to 2×10^{24} cm^{-2} in the current sample. This corresponds to $A_V \sim 30$–1000, (Seward 2000). Values of N_H(int) determined for the nine low-count sources (encircled in Figure 4) using the models in that figure are listed in Table 3.

4.3. X-Ray and Mid-IR Properties

Spitzer observations of the high-redshift 3CRR sample (Haas et al. 2008) demonstrate uniform power law plus silicate emission SEDs for the quasars while the NLRGs show a variety of SED shapes. The latter are interpreted in terms of a range of quasar to host galaxy ratios and absorption properties. Quasars and NLRGs separate well in the optical depth of 9.7 μm silicate absorption ($\tau_{9.7\,\mu m}$), with the NLRGs having higher values (Leipski et al. 2010). The level of $\tau_{9.7\,\mu m}$ also tracks the source orientation (R_{CD}). The one exception in this sample is 3C 190, a CSS quasar with significant silicate absorption ($\tau_{9.7\,\mu m} = 0.60$, see Section 5.3).

X-ray absorption column densities are often significantly higher than those in the visible or IR (factors of 3–100; Maiolino et al. 2001), implying differing lines of sight, low gas-to-dust ratios perhaps due to high temperatures in the material close to the nucleus, or a lack of small grains in the nuclear dust (Gaskell et al. 2004). A reported correlation between the strength of the silicate absorption feature and estimated X-ray absorption (Shi et al. 2006) indicates ∼100× higher X-ray (gas) column density. Figure 6 shows the X-ray hardness (left) and the estimated N_H(int) (right) as a function of $\tau_{9.7\,\mu m}$ from Leipski et al. (2010). Relative to an average quasar spectrum, which includes silicate 9.7 μm emission, the NLRGs, including those with soft hardness ratios, show significant $\tau_{9.7\,\mu m}$. This implies that gas (X-ray absorption) and dust (IR absorption) are related. However, the intermediate sources, 3C 68.1/325,[14] look like quasars in the IR, with no significant $\tau_{9.7\,\mu m}$ and inconsistent with a detailed gas/dust spatial correlation. Tests show a significant correlation of $\tau_{9.7\,\mu m}$ with X-ray N_H(int) in the current sample ($P < 0.0001$; Kendall's τ test).

The three sources with the highest $\tau_{9.7\,\mu m}$ ($\gtrsim 1$) are well separated from the remainder of the galaxies in Figure 6. Of these, two X-ray soft NLRGs 3C 324/368 are known to be located in edge-on host galaxies (Best et al. 1998; Laskar et al. 2010), supporting earlier suggestions that the host galaxy contributes significantly to the IR obscuration in active galaxies and quasars (Goulding et al. 2012; Deo et al. 2009). The optical data for the third, NLRG 3C 469.1, are of too low quality to confirm a similar edge-on view, but the extended, aligned radio and X-ray emission (Laskar et al. 2010) are suggestive.

Figure 7 shows X-ray HR (left) and N_H(int) (right) as a function of rest-frame $L_{5\,\mu m}/L_{8\,\mu m}$[15], which is also demonstrated to be an absorption indicator (Haas et al. 2008). Quasars are relatively unabsorbed with high $L_{5\,\mu m}/L_{8\,\mu m}$ while NLRGs are absorbed with lower values. While the X-ray and IR absorption appear to be related, there is no significant correlation with

[14] The third, 3C 241, was not observed with the *Spitzer* IRS.

[15] k-corrected based on the observed slope between 8 μm (IRAC) and 24 μm (MIPS).

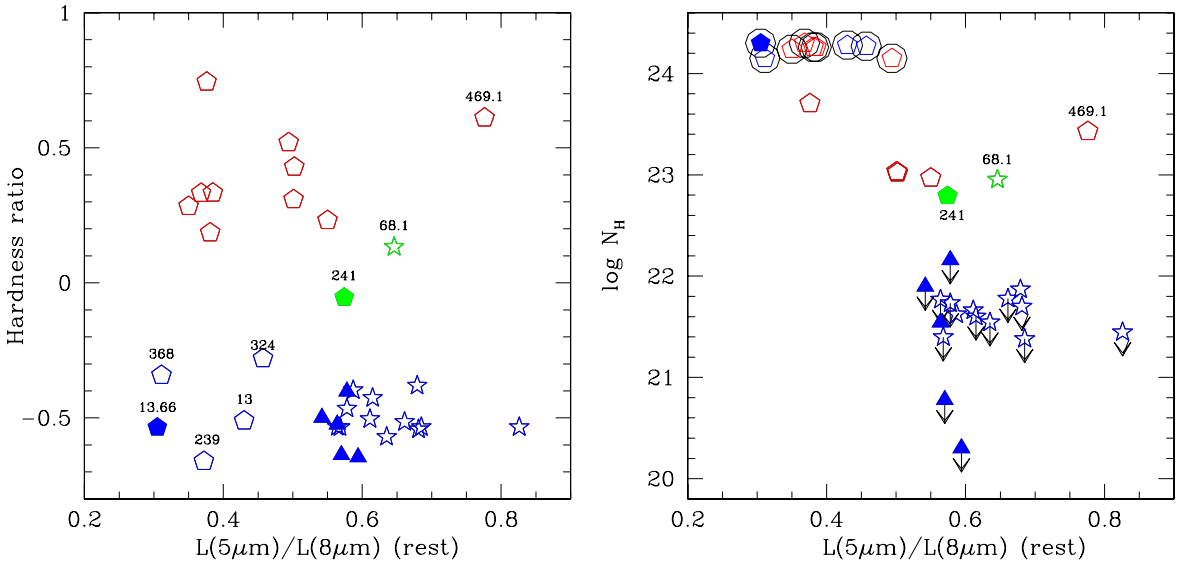

Figure 7. X-ray hardness ratio (HR, left) and the equivalent intrinsic hydrogren column density ($N_{\rm H}$(int), right) estimated from spectral fits or $L_{\rm X}$ (circled data points) as a function of the ratio of intrinsic 5 μm to 8 μm luminosities ($L_{5\,\mu{\rm m}}/L_{8\,\mu{\rm m}}$). NLRG 3C 469.1 looks blue in $L_{5\,\mu{\rm m}}/L_{8\,\mu{\rm m}}$because the deep $\tau_{9.7\,\mu{\rm m}}$ absorption affects the observed 24 μm band at redshift, $z = 1.336$. The colors and symbols are as in Figure 5.

(A color version of this figure is available in the online journal.)

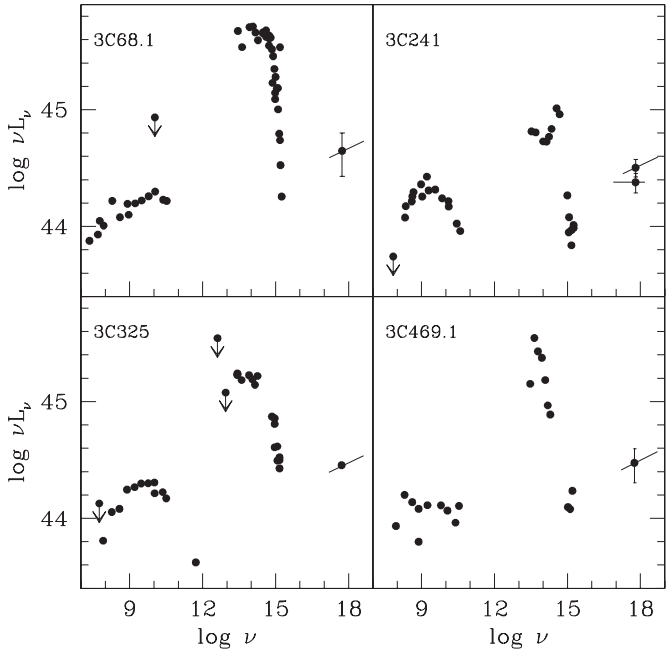

Figure 8. Radio–X-ray spectral energy distributions (SEDs) of the intermediate QSO/NLRG sources as labeled in each panel and the unusual source 3C 469.1. Upper limits are indicated at 3σ and the X-ray points indicate the estimated spectral slopes. All four sources have a red optical–UV continuum with little evidence for a blue bump indicating strong UV absorption. The lack of visible galaxy emission is consistent with the observed moderate X-ray absorption, $N_{\rm H} \sim 10^{22-23}$ cm^{-2}. 3C 469.1 also has strong $\tau_{9.7\,\mu{\rm m}}$ absorption.

either X-ray HR or $N_{\rm H}$(int). The intermediate sources have quasar-like $L_{5\,\mu{\rm m}}/L_{8\,\mu{\rm m}}$. NLRG 3C 469.1 is once again unusual. It has very strong silicate absorption so that the derived rest-frame $L_{5\,\mu{\rm m}}/L_{8\,\mu{\rm m}}$ is unusually blue (Figure 7). Apart from this anomaly, the IR and visible SED of 3C 469.1 (Figure 8) is red and consistent with that of an NLRG (Leipski et al. 2010).

The near-IR obscuration of the NLRGs deduced from the $L_{5\,\mu{\rm m}}/L_{8\,\mu{\rm m}}$ ratio indicates an average obscuration $A_{\rm V} \sim 50$ (Haas et al. 2008), while that indicated by $\tau_{9.7\,\mu{\rm m}}$ is lower, $A_{\rm V} \sim 20$ (Leipski et al. 2010). The X-ray data imply $A_{\rm V} \sim$ 30–1000, again showing the tendency for the X-ray absorption to be higher. The difference in the two IR absorption indicators suggests that the hot dust component ($\sim$4 μm) is closer to the AGN than the MIR emission/absorption region (Deo et al. 2011).

4.4. Radio Core Fraction

As noted earlier, at low frequencies all the 3CRR sources are lobe dominated, but at higher frequencies emission from the core becomes significant. The relative strength of the core emission (core fraction, $R_{\rm CD}$) can be used as an orientation indicator. Unification models predict a correlation between obscuration and orientation. Figure 9 (left) shows $L_{\rm X}/L_{\rm R}$ as a function of $R_{\rm CD}$ with X-ray hardness ratio indicated by color. A strong correlation is present ($P_{\rm null} = 0.0001$, generalized Kendall's τ test including upper limits on $R_{\rm CD}$), consistent with unification models (see also Donley et al. 2005 for lower-redshift RLAGNs). The orientation dependence of the beamed, core emission is likely to also contribute to this relation. The significant relation between $N_{\rm H}$(int) and $R_{\rm CD}$ ($P_{\rm null} = 0.0001$, Kendalls' τ test) shown in Figure 9 (right) also strongly supports unification models.

5. DISCUSSION

5.1. Compton Thick (CT) Candidates

Four of the *Chandra*-observed NLRGs, 3C 13/324/368, and 4C 13.66, have soft X-ray hardness ratios consistent with a clear line of sight to a face-on quasar while their X-ray luminosities are low, comparable to the other NLRGs. The count rates are sufficiently low that spectral fits provide no useful constraint on intrinsic column density for these sources (Table 2). There are two possible interpretations. First, they could be LERGs that have little/no X-ray absorption and lack an actively accreting AGN (Section 1.2), but since the current sample is high luminosity this is unlikely. Second, the direct

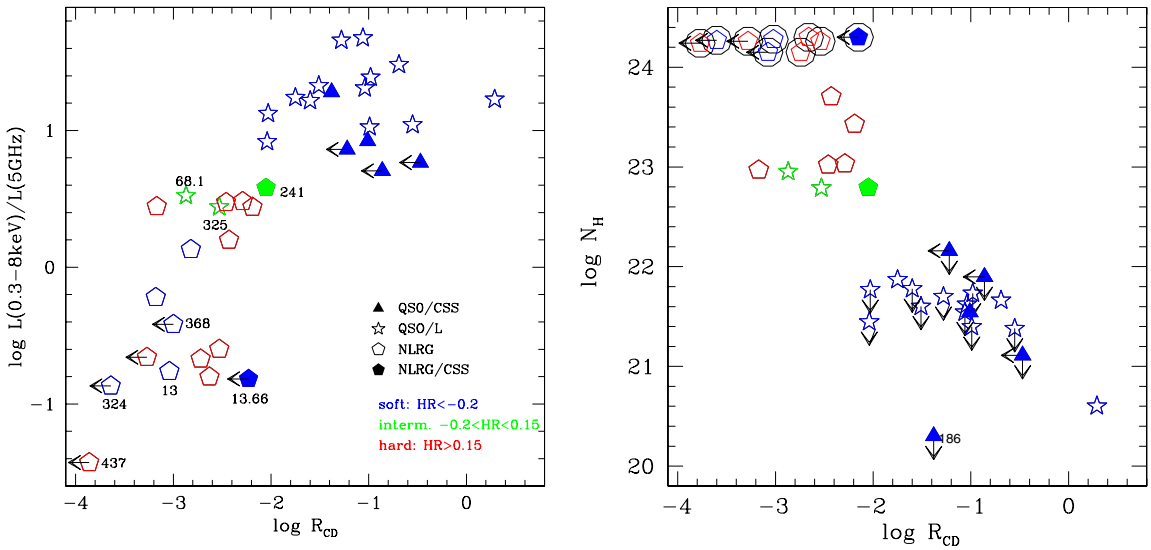

Figure 9. X-ray to total radio luminosity ratio (L_X/L_R, left) and intrinsic equivalent hydrogen column density (N_H(int), right) estimated from spectral fits or L_X (circled data points) as a function of the radio core fraction R_{CD}. A strong relation with R_{CD} is present for both parameters consistent with the orientation-dependent obscuration of unification models.

(A color version of this figure is available in the online journal.)

AGN light in the soft NLRGs may be sufficiently absorbed (CT) that the observed X-rays are dominated by other, relatively weak components, as observed in red quasars (Kuraszkiewicz et al. 2009a) and consistent with the models in Figure 4.

The circumnuclear regions of AGNs are rarely resolved, particularly at high redshift, and so the extracted X-ray counts will include contributions such as nuclear light scattered into our line of sight via dust/electrons above/below the AD/torus, extended X-ray emission due to photo- or collisional-ionization in material surrounding the nucleus, and/or non-thermal emission from extended radio structure. NGC 1068 is the archetypal CT source for which the X-ray emission was measured to be weak and soft in low spatial resolution data (Monier & Halpern 1987). Detailed *Chandra* and *XMM-Newton* data have since revealed extended soft X-ray emission and a complex X-ray spectrum including multiple reflected components (Matt et al. 2000; Pounds & Vaughan 2006; Ogle et al. 2003). Although there are too few source counts in the soft NLRGs to study source extent, counts were extracted from a smaller (1″ radius) circle to test this possibility. For 3C 324/368, the *Chandra* data show extended X-ray emission over a larger region and the resulting nuclear spectrum is harder (Table 2, footnote k; Figure 5), consistent with contamination by softer extended emission. The lack of similar spectral hardening for 3C 13 and 4C 13.66 does not rule out the presence of unresolved extended soft emission.

The luminosity of the [O III]λ5007 emission line (hereafter L[O III]) tracks the radio and X-ray luminosities for broad- and narrow-lined AGNs (Jackson & Rawlings 1997; Mulchaey et al. 1994), and at high luminosities there is little/no inclination dependence (see discussion in Section 1.2). Given the strong dependence of the observed X-ray flux on obscuration, L[O III] is often used as an indicator of the intrinsic X-ray luminosity, and the ratio of the two quantities indicates whether or not a source is CT (Risaliti et al. 1999; Panessa et al. 2006). Figure 10 shows the ratio L[O III]/L_X[16] as a function of R_{CD} for the 3CRR sample

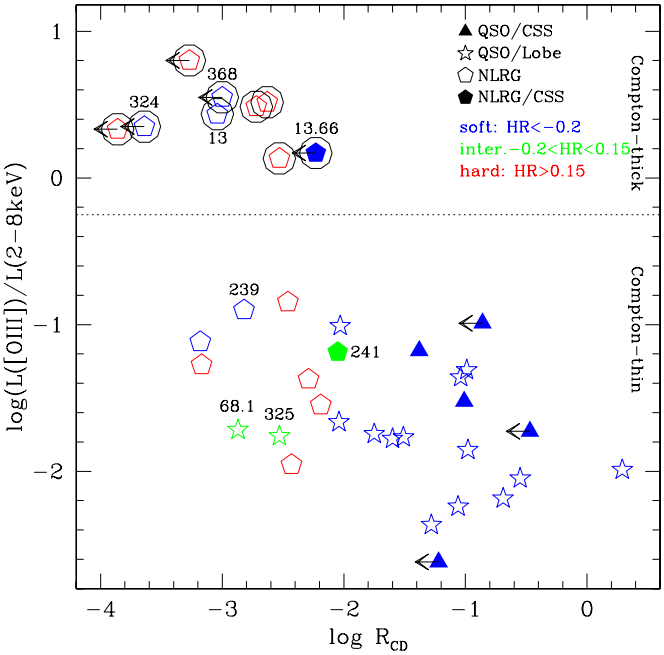

Figure 10. Ratio of L[O III] to hard (2–8 keV) X-ray luminosity (not corrected for N_H(int)) as a function of radio core fraction R_{CD}. The symbols and colors are indicated in the legend. For five sources with no measured L[O III] (3C 43/204/325/437/469.1), values were estimated from measurements of L[O II] following Grimes et al. (2004). Nine NLRGs lie in the range of L[O III]/L_X expected for Compton thick (CT) AGNs as indicated by the dotted line (Juneau et al. 2011).

(A color version of this figure is available in the online journal.)

in comparison with the CT criterion of Juneau et al. (2011). Any weakening of the observed L[O III] due to obscuration of the inner NLR would imply a larger intrinsic L[O III]/L_X. All four of the *Chandra*-observed X-ray soft NLRGs have high L[O III]/L_X ratios, consistent with CT X-ray emission. Five additional NLRGs 3C 68.2/266/294/356/437 are also CT by this criterion. They have HRs ∼ 0.2–0.4 (Table 2) but their L_X values are comparable with the soft NLRGs and, in comparison with the models (Figure 4), indicate $N_H(\mathrm{int}) \gtrsim 1.5 \times 10^{24}$ cm^{-2} (Table 3).

[16] L[O III] measurements are from Grimes et al. (2004). For 3C 43/204/325/437/469.1 L[O III] was determined from L[O II] using the relation reported in that paper.

Another parameter suggested to be a CT indicator is $\tau_{9.7\,\mu m}$ (Georgantopoulos et al. 2011). There are three sources with $\tau_{9.7\,\mu m} > 1$: 3C 324/368/469.1 (Figure 6; Section 4.3), adding 3C 469.1 as a CT candidate. However, not all properties of this source align with a CT interpretation. 3C 469.1 has a relatively high L_X, a hard X-ray spectrum (Figure 5), $N_H(\mathrm{int}) \sim 3 \times 10^{23}$ cm^{-23} (Table 2), and low $L[\mathrm{O\,III}]/L_X$ (Figure 10). Although we cannot rule out that this source is intrinsically different, it seems most likely that the nuclear absorption is not CT and that the unusually high $\tau_{9.7\,\mu m}$ is dominated by the host galaxy. Three other CT candidates 3C 13/256/266 have significant $\tau_{9.7\,\mu m} > 0.5$, while the remainder do not have the IRS data required to measure this feature.

The NLRG 3C 239, observed by *XMM-Newton*, has a soft X-ray spectrum and possible Fe Kα emission, leading Salvati et al. (2008) to suggest it is a CT source. The *Spitzer* $L_{5\,\mu m}/L_{8\,\mu m}$ flux ratio aligns with the other soft NLRGs (Figure 7). However, the radio core fraction indicates an intermediate orientation (Figure 9), L_X is significantly higher than the other soft NLRGs (Figure 5), and the low $L[\mathrm{O\,III}]/L_X$ ratio places it well inside the Compton-thin region (Figure 10). Optical imaging shows a complex structure suggestive of a merger remnant (Best et al. 1997). Given the conflicting properties and the relatively low S/N of the *XMM-Newton* data,[17] this source is not included in the list of CT candidates. The unusual combination of soft X-ray spectrum and intermediate X-ray luminosity (Figure 5) suggest an intermediate level of absorption combined with significant soft excess emission. Deeper X-ray data are required to confirm/refute this suggestion.

The *Chandra* spectrum of the NLRG 3C 294 was studied at higher S/N by Fabian et al. (2003b), who report that it is dominated by a disk reflection component and deduce $N_H = (8.4 \pm 1) \times 10^{23}$ cm^{-1}, within 2σ of being CT, and an intrinsic $L_X \sim 1.1 \times 10^{45}$ erg cm^{-2} s^{-1}. We thus consider the evidence that this source is CT to be marginal, and it is not included in our final CT list.

We conclude that there are 8 CT candidates among the 16 NLRGs (not including the intermediate source 3C 241 as an NLRG; Section 5.2) in this sample. We used the CIAO/Sherpa extension package Datastack to perform simultaneous X-ray spectral fits to the eight data sets to explore their spectral form since individual fits provided no constraints on the spectral parameters (Section 3). Datastack allows the source redshifts and calibration files of the individual observations to be used appropriately during simultaneous fitting of a group of sources. The results confirm that no significant $N_H(\mathrm{int})$ is detected and that a power law provides a good fit ($\Gamma \sim 1.6$). However, since the total number of counts for all eight sources is 150, the fit does not provide strong constraints on the presence of a reflection component.

The eight CT sources represent $\sim$21% $\pm$ 7% of the 3CRR sources in this redshift range. Of these sources, five are well-documented aligned radio galaxies with extended optical/IR emission distributed along the radio axis: 3C 13 (Best et al. 1997), 3C 266 (Zirm et al. 2003), 3C 324 and 3C 368 (Best et al. 1998), and 4C 13.66 (Rawlings et al. 1996), although this last is very small (1″.4) on the sky and the optical extension is not well defined. The predominantly edge-on nature of these candidates for CT nuclear absorption suggests that the host galaxy may contribute significantly to the absorption (Goulding et al. 2012; Deo et al. 2009; Kuraszkiewicz et al. 2009b).

[17] Such that the Fe Kα emission line is within 2σ of the normal strength for a type 1 AGN (G. Risaliti 2012, private communication).

5.2. Intermediate Quasars and NLRGs

Two of the quasars (3C 68.1/325) are unusually hard in the X-ray compared with the remainder of the 3CRR quasars (Figure 4). Their X-ray properties, along with those of NLRG 3C 241, are intermediate between those of NLRGs and quasars (Section 4.2).

3C 68.1 has hard X-ray emission, while the silicate absorption at 9.7 μm is weak and in the quasar range (Leipski et al. 2010). The SED (Figure 8) shows a red optical/near-IR continuum and little/no blue bump. The optical spectrum includes broad and narrow emission lines and strong, narrow absorption close to the emission-line redshift ($v \sim -70$ km s^{-1}; Brotherton et al. 1998). The optical continuum and broad lines are highly polarized, ranging from $\sim$5%–10%, progressing from red to blue along the spectrum. The combination of high polarization, no strong variability, broad lines, weak (undetected in the ROSAT All-Sky Survey) X-rays, and strong UV absorption was interpreted by Brotherton et al. (1998) as due to an inclined system where the scattered, polarized emission is diluted by dust-reddened direct light toward the red end of the optical spectrum. The *Chandra* detection shows relatively weak X-ray emission obscured by an intermediate absorbing column density ($N_H(\mathrm{int}) \sim 9 \times 10^{22}$ cm^{-22}; Table 2), confirming this picture.

3C 325, originally classified as an NLRG, was re-classified as a quasar based on the presence of weak broad components to the optical emission lines (Grimes et al. 2005). That paper also updated the redshift to 1.135 (earlier reported to be 0.86). The *Spitzer* IR data confirm the re-classification, showing the strong, smooth, power-law-like continuum and silicate emission that are characteristic of the 3CRR quasars (Leipski et al. 2010). The SED (Figure 8) shows a red optical/near-IR continuum and little/no blue bump. The *Chandra* data show relatively weak X-ray emission and intermediate absorption column density ($N_H(\mathrm{int}) \sim 6 \times 10^{22}$ cm^{-2}; Table 2).

3C 241 is classified as an NLRG/CSS, but a broad Hα line has been observed in this source (Hirst et al. 2003), implying that it is also intermediate between quasars and NLRGs. The SED (Figure 8) shows a red optical/near-IR continuum and approximately no blue bump. There are no *Spitzer* IRS data for this source. The *Chandra* data again show relatively weak X-ray emission and intermediate absorption column density ($N_H(\mathrm{int}) \sim 6 \times 10^{22}$ cm^{-2}; Table 2).

The multi-wavelength properties of all three sources are very similar to those of red AGNs and suggest type 1 quasars with an intermediate level of obscuration so that the X-ray flux remains relatively strong (Wilkes et al. 2002, 2005). The AGN IR bump outshines the host galaxy emission but the optical/UV emission is largely obscured (Kuraszkiewicz et al. 2009a).

Numerous hybrid sources whose classification as type 1 or 2 AGNs depends on the observed waveband have been reported over the years. Galaxies bright in the IR and dominated by a starburst may contain an AGN. AGNs with narrow lines in the optical reveal broad lines in IR observations or in polarized optical light. Specific AGN classes include X-ray bright, optically normal galaxies (Georgantopoulos & Georgakakis 2005) or optically dull AGNs (Elvis et al. 1981), red quasars (e.g., 2MASS sample; Cutri et al. 2002), and type 2 quasars (Zakamska et al. 2008; Ptak et al. 2006). Explanations include an evolutionary stage in which a quasar is emerging from an early, enshrouded state (Hopkins et al. 2006; Sanders et al. 1988), an intermediate orientation of the AGN in which the quasar is viewed through a lower column density of material and/or an edge-on host galaxy(Kuraszkiewicz et al. 2009a,

2009b; Wilkes et al. 2002; Elvis 2000), dilution by a bright and/or edge-on host galaxy, or an intrinsically weak AGN (Trump et al. 2009; Hopkins et al. 2009). Since this is a luminous, radio-selected sample, the last two possibilities, which imply a weak AGN, seem unlikely. While an evolutionary stage with a weak AGN cannot be ruled out, we will see below (Figure 9) that the core fraction of these three sources supports an intermediate viewing angle with a lower column density of obscuring material. This would be identified with a corona/wind above or below the AD/torus as posited in current models (Elvis 2000; Konigl & Kartje 1994) or a relatively clear line of sight in a clumpy torus model (Nenkova et al. 2008).

5.3. Compact Steep Spectrum (CSS) Sources

The 3CRR sample includes eight CSS sources: six are classified as quasars, one as an NLRG (CT candidate 4C 13.66), and one as an intermediate source (3C 241). The radio source size is smaller than a typical galaxy, and models generally involve a young radio source in a later stage than the GHz peaked sources (GPS), which tend to be smaller with radio structure comparable in size to the NLR (O'Dea 1998). The lack of X-ray absorption in *Chandra* observations of both GPS and CSS sources (Siemiginowska et al. 2008) rules out earlier models in which the radio source was confined by interaction with a surrounding medium. Their X-ray properties are consistent with unification: the quasars are not heavily obscured while the NLRGs are. The small radio size then indicates that they are young rather than confined by an external medium whose presence would be clear from additional X-ray absorption (Siemiginowska et al. 2008). However, comparison of the X-ray properties of a well-defined sample of GPS sources with a heterogeneous sample of radio galaxies and quasars suggests that GPS sources are X-ray weak (by a factor ∼10) and somewhat obscured (Tengstrand et al. 2009).

Our sample provides a well-matched set of CSS and other radio sources. Their X-ray properties generally align with those of the rest of the sample. The quasars show no absorption, the NLRG 4C 13.66 is a CT candidate, and the intermediate source 3C 241 is similar to the other two in that category (Figure 4). Figure 5 shows that the CSS quasars are at the low end of the L_X/L_R range for quasars. The mean ratio for CSS quasars is a factor of 2.5 lower than that for the rest of the quasars due to a combination of higher L_R(5 GHz) and lower L_X. The fitted X-ray slopes for the two sources with sufficient counts (Table 2) are relatively soft, $\Gamma \sim 1.8$ (3C 287) and $\Gamma \sim 2.1$ (3C 186, see also Siemiginowska et al. 2008), compared with the other quasars (mean $\Gamma \sim 1.7$). Thus, the X-ray properties of this uniform set of CSS quasars support earlier conclusions that the radio sources are young rather than confined. The CSS quasars have L_X/L_R values a factor of ∼2.5 lower than the well-matched quasars in this sample, a smaller shift than that reported by Tengstrand et al. (2009). The combination of lower L_X/L_R and softer X-ray slopes could result from weaker jet-related X-ray emission, but a larger well-matched sample is needed to confirm a systematic discrepancy.

3C 190 is a CSS quasar with conflicting properties. The X-ray properties align with the other CSS quasars, but the IR data indicate silicate absorption ($\tau_{9.7\,\mu m} \sim 0.6$; Leipski et al. 2010) rather than the typical emission. This measurement was made with respect to the silicate emission from an average quasar so that an alternative interpretation is of weak/absent silicate emission. It has been suggested (Leipski et al. 2010; P. Ogle et al., in preparation) that CSS quasars may have unusual silicate features, although the other CSS quasars in the current sample have silicate emission similar to normal quasars, not supporting this idea. Other possibilities include significant host galaxy absorption or a complex X-ray spectrum so that the deduced low N_H(int) is incorrect.

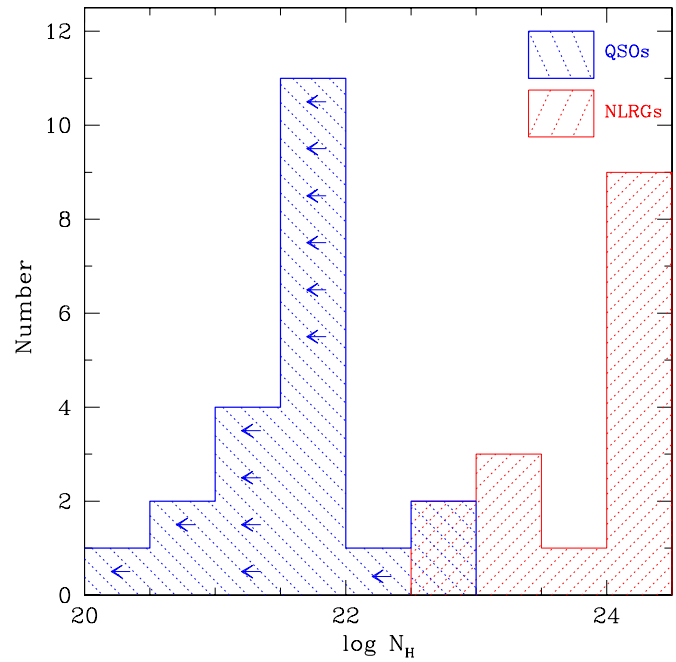

Figure 11. Distribution of the best estimates of X-ray equivalent intrinsic hydrogen column density for the *Chandra*-observed sample. Quasars are shown in red and NLRGs in blue with upper limits, mostly for quasars with no evidence for intrinsic absorption, indicated by arrows.

(A color version of this figure is available in the online journal.)

5.4. The Distribution of Intrinsic X-Ray Absorption Column Densities

The best estimates of the intrinsic absorption column densities, N_H(int), for the 3CRR sources (Tables 2 and 3) were determined with reference to both X-ray and multi-wavelength properties of each source (Section 4.2). The resulting N_H(int) distribution is bi-modal (Figure 11) with N_H(int) for the NLRGs peaking at $>10^{24}$ cm^{-2}. A similar distribution, with obscured sources peaking $>3\times10^{23}$ cm^{-2}, was reported for lower-redshift 3CRR galaxies ($z < 1$; Evans et al. 2006; Hardcastle et al. 2009, their Figure 16). In that case, the N_H(int) is based on spectral fits that include two power-law components, one of which (accretion related) is absorbed while the other (radio jet related) is not. The current *Chandra* data are not of sufficiently high S/N to allow the multi-component fitting used in the low-redshift sample. Despite the different analysis, the similarity of the two distributions reinforces the earlier conclusion that the N_H(int) distribution for radio-selected AGNs extends to higher values than that of type 2 sources found in the Sloan Digital Sky Survey. Distributions derived for lower-luminosity, local Seyfert 2 galaxies are more similar (Risaliti et al. 1999). Once again, this result emphasizes that low-frequency radio selection includes the full population, including the highly obscured (edge-on) sources that selection in other wavebands preferentially misses.

Low S/N observed X-ray spectra do not accurately reflect the true level of obscuration for highly obscured sources. Even in the high-luminosity 3CRR sample, some objects display weak

and soft X-ray emission because the primary X-ray power law is sufficiently obscured that weaker X-ray components dominate. Using HRs or simple power-law fits to estimate the absorption column densities may yield values 10–1000× too low and lead to intrinsic X-ray luminosities ∼10–100× below the true values. Underestimated absorption would result in an apparent lack of heavily obscured sources in X-ray-selected AGN samples because such sources either appear to be unabsorbed, adding to the unobscured rather than the obscured source counts, or they fall below the flux limit and are missing from the sample altogether.

From the distribution of $N_{\rm H}$(int), we conclude that the obscured fraction in the high-z 3CRR sample is 0.5 ± 0.1 and the CT fraction is 0.21 ± 0.07, both consistent with CXRB model predictions in this range of $L_{\rm X}$ (Gilli et al. 2007). This obscured fraction is higher than is typically reported for sources in the same luminosity range (∼0.1–0.3, see Section 1.2), a discrepancy that can be explained if the ∼20% CT sources are generally either undetected or accounted as unobscured. Similar CT fractions (∼0.18) have been reported for $z > 3$, lower $L_{\rm X}$ (log $L_{\rm X} \sim$ 43–44) X-ray-selected sources in the CDFS (Fiore et al. 2012) and in low-redshift ($z < 0.1$) hard X-ray surveys (Burlon et al. 2011). In summary, the ratio of unobscured to Compton thin ($10^{22} < N_{\rm H}$(int) $< 1.5 \times 10^{24}$ cm^{-2}) to CT ($N_{\rm H}$(int) $> 1.5 \times 10^{24}$ cm^{-2}) is 2.5:1.4:1 for the high-z 3CRRs.

5.5. Geometry of the Nuclear Region

The strong relations between the X-ray to radio luminosity ratio ($L_{\rm X}/L_{\rm R}$) and the intrinsic absorption column density ($N_{\rm H}$(int)) and the AGN orientation as indicated by $R_{\rm CD}$ (Figure 9) confirm that orientation-dependent obscuration dominates the nuclear X-ray and core radio properties of high-redshift RLAGNs, supporting the unification model. Anomalously high $\tau_{9.7\,\mu{\rm m}}$ in a few sources indicates that the host galaxy makes significant contributions to the SEDs when the spatial resolution is insufficient to isolate the nuclear emission.

Estimates of the number of sources as a function of the amount of obscuration provide constraints on the covering factor of the material in the nuclear regions immediately surrounding the central SMBH. Half of the sample (19 of 38) are type 1 sources (obscured fraction of 0.5) with little or no X-ray absorption, strong, broad emission lines, and blue visible colors. This is consistent with previous estimates for samples of radio galaxies once the LERGs are removed (Barthel 1989; Ogle et al. 2006). Assuming randomly oriented 3CRR sources and a geometry in which the obscuring material lies preferentially in a plane perpendicular to the radio jet, the probability of a source lying in a cone of angle ϕ is given by $P(\theta < \phi) = 1 - \cos\phi$ (Barthel 1989), leading to an estimated half-opening angle for the obscuring material of $60^\circ \pm 8^\circ$.

The 3CRR sample includes eight CT candidate NLRGs with one/more of the following properties: low X-ray luminosity ($L_{\rm X}/L_{\rm R}$, sometimes accompanied by soft X-ray spectra), high [O III]λ5007 to X-ray luminosity ratio, low $R_{\rm CD}$, high $\tau_{9.7\,\mu{\rm m}}$. In a unification scenario, these are the highest inclination sources, viewed through the optically thick material of the AD/torus so that only weaker emission, reflected/scattered from cold and/or warm (ionized) material outside the nucleus, is visible in the X-rays, i.e., similar to the archetypal edge-on AGN NGC 1068. The CT candidates represent 50%±18% (8 of 16) of the NLRGs in this sample. Six of these sources are also in edge-on or merging host galaxies, suggesting that host galaxy obscuration also plays a role. With 21% ± 6% of the total sample in this category, we estimate that the CT torus/AD covers $12^\circ \pm 4^\circ$ above and below the equatorial plane of the system.

The remaining eight NLRGs and the three intermediate sources[18] (Section 5.2) have Compton-thin $N_{\rm H}$(int) and intermediate $L_{\rm X}/L_{\rm R}$ and $R_{\rm CD}$. This group constitutes 29% ± 7% of the sample, indicating obscuration above and below the CT disk covering a further $18^\circ \pm 3^\circ$. The presence of three intermediate-class sources suggests that the material decreases in density away from the plane of the disk, perhaps including an atmosphere/wind (Konigl & Kartje 1994; Murray & Chiang 1995).

6. CONCLUSIONS

1. *Chandra* X-ray observations of a complete sample of 38 high-redshift ($1 \lesssim z \lesssim 2$) 3CRR radio sources (log $L_{\rm R}$(5 GHz) ∼ 44–45, log $L_{\rm X}$ ∼ 43–46) combined with multi-wavelength data have demonstrated that source orientation can explain the full range of X-ray properties, consistent with the orientation-dependent obscuration of the unification model for RL quasars and radio galaxies (NLRGs).
2. The obscured fraction for this sample of high-redshift 3CRR sources is 0.5 ± 0.1, consistent with that expected at log $L_{\rm X}$ ∼ 45–46 in CXRB models (Gilli et al. 2007), but higher than that generally reported at these luminosities (0.1–0.3). The difference is most likely due to the lack of bias against obscured sources in the low-frequency radio-selected 3CRR sample.
3. The multi-wavelength properties of many of the 3CRR NLRGs reveal significantly (10–1000×) higher levels of intrinsic absorption ($N_{\rm H}$(int)) than indicated by the X-ray hardness ratios. In such cases, the use of X-ray hardness ratio to correct for $N_{\rm H}$(int) results in $L_{\rm X}$ values ∼10–100× too low.
4. We conclude that eight of the NLRGs (50% ± 18%) are CT (3C 13/68.2/266/324/356/368/437 and 4C 13.66). The high fraction of CT sources (21%) compared with visible and X-ray-selected samples is a result of the lack of bias against heavily obscured sources via radio-selection. The ratio of unobscured to Compton-thin ($10^{22} < N_{\rm H}$(int) $< 1.5 \times 10^{24}$ cm^{-2}) to CT ($N_{\rm H}$(int) $> 1.5 \times 10^{24}$ cm^{-2}) is 2.5:1.4:1.
5. Assuming a random distribution of orientation and a simple geometry in which the obscuring material is concentrated perpendicular to the radio axis, we deduce that obscuration in the nuclear regions of high-z RLAGNs includes a CT obscuring disk/torus extending ∼12° from the midplane, additional obscuring material extending for another ∼18° with the density decreasing away from the mid-plane, and the remaining ∼60° is largely unobscured. This last is consistent with previous estimates of torus/disk opening angles for high-luminosity AGNs.
6. $L_{\rm X}/L_{\rm R}$ and L[O III]$/L_{\rm X}$, in comparison with typical values for broad-line AGNs, provide a better measure of intrinsic absorption than the X-ray HR.
7. The distribution of $N_{\rm H}$(int) for the high-redshift 3CRR sample peaks at $N_{\rm H}$(int) $> 10^{24}$ cm^{-2}, similar to the results for lower-redshift 3CRR sources.

[18] The optical and IR spectral data for many of the NLRGs, which are very faint optical sources, are of low S/N making weak broad lines difficult to detect so that the NLRG vs. intermediate classification is non-uniform.

8. Given the edge-on nature of the host galaxies of at least five of the CT NLRGs (3C 13/266/324/368 and 4C 13.66), it is likely that host galaxy absorption contributes significantly to dust absorption signatures such as $\tau_{9.7\,\mu\mathrm{m}}$.
9. The CSS RLAGNs (3C 43/186/190/241/287/318/454.0 and 4C 13.66) have a factor of $\sim$2.5 lower $L_{\mathrm{X}}/L_{\mathrm{R}}$ and softer X-ray spectra ($\Gamma \sim 1.8$–2 cf. 1.7) than the non-CSS RLAGN in this complete sample.

Support for this work was provided by the National Aeronautics and Space Administration through *Chandra* Award Number G08-9106X, by the Chandra X-Ray Center, which is operated by the Smithsonian Astrophysical Observatory for and on behalf of the National Aeronautics Space Administration under contract NAS8-03060 (Chandra X-Ray Center) and by the Smithsonian Institution Endowment, Scholarly Studies Program, fund 40488100HH0017. The scientific results in this article are based to a significant degree on observations made by the *Chandra X-Ray Observatory* (*CXO*). We thank Mark Avara and Margaret Yellen for their early work on this project.

REFERENCES

Akujor, C. E., & Garrington, S. T. 1995, A&AS, 112, 235
Akujor, C. E., Luedke, E., Browne, I. W. A., et al. 1994, A&AS, 105, 247
Akujor, C. E., Spencer, R. E., Zhang, F. J., et al. 1991, MNRAS, 250, 215
Aldcroft, T. L., Siemiginowska, A., Elvis, M., et al. 2003, ApJ, 597, 751
Antonucci, R. R. J. 1984, ApJ, 278, 499
Antonucci, R. R. J., & Miller, J. S. 1985, ApJ, 297, 621
Barmby, P., Alonso-Herrero, A., Donley, J. L., et al. 2006, ApJ, 642, 126
Barthel, P., Haas, M., Leipski, C., & Wilkes, B. 2012, ApJL, 757, L26
Barthel, P. D. 1989, ApJ, 336, 606
Barthel, P. D., Miley, G. K., Schilizzi, R. T., & Preuss, E. 1984, A&A, 140, 399
Bassani, L., Molina, M., Malizia, A., et al. 2006, ApJL, 636, L65
Belsole, E., Worrall, D. M., & Hardcastle, M. J. 2006, MNRAS, 366, 339
Belsole, E., Worrall, D. M., Hardcastle, M. J., Birkinshaw, M., & Lawrence, C. R. 2004, MNRAS, 352, 924
Best, P. N., Carilli, C. L., Garrington, S. T., Longair, M. S., & Rottgering, H. J. A. 1998, MNRAS, 299, 357
Best, P. N., Longair, M. S., & Roettgering, J. H. A. 1997, MNRAS, 292, 758
Best, P. N., Röttgering, H. J. A., & Longair, M. S. 2000, MNRAS, 311, 23
Bridle, A. H., Hough, D. H., Lonsdale, C. J., Burns, J. O., & Laing, R. A. 1994, AJ, 108, 766
Brotherton, M. S., Wills, B. J., Dey, A., van Breugel, W., & Antonucci, R. 1998, ApJ, 501, 110
Burlon, D., Ajello, M., Greiner, J., et al. 2011, ApJ, 728, 58
Cappi, M., Panessa, F., Bassani, L., et al. 2006, A&A, 446, 459
Chiaberge, M., Capetti, A., & Celotti, A. 2002, A&A, 394, 791
Cleary, K., Lawrence, C. R., Marshall, J. A., Hao, L., & Meier, D. 2007, ApJ, 660, 117
Cutri, R. M., Nelson, B. O., Francis, P. J., & Smith, P. S. 2002, in ASP Conf. Ser. 284, IAU Colloq. 184: AGN Surveys, ed. R. F. Green, E. Y. Khachikian, & D. B. Sanders (San Francisco, CA: ASP), 127
Daddi, E., Dickinson, M., Morrison, G., et al. 2007, ApJ, 670, 156
Davis, M., Guhathakurta, P., Konidaris, N. P., et al. 2007, ApJL, 660, L1
Deo, R. P., Richards, G. T., Crenshaw, D. M., & Kraemer, S. B. 2009, ApJ, 705, 14
Deo, R. P., Richards, G. T., Nikutta, R., et al. 2011, ApJ, 729, 108
Dicken, D., Tadhunter, C., Axon, D., et al. 2009, ApJ, 694, 268
Dickey, J. M., & Lockman, F. J. 1990, ARA&A, 28, 215
Donley, J. L., Koekemoer, A. M., Brusa, M., et al. 2012, ApJ, 748, 142
Donley, J. L., Rieke, G. H., Rigby, J. R., & Pérez-González, P. G. 2005, ApJ, 634, 169
Dwelly, T., & Page, M. J. 2006, MNRAS, 372, 1755
Eisenhardt, P. R., Stern, D., Brodwin, M., et al. 2004, ApJS, 154, 48
Elvis, M. 2000, ApJ, 545, 63
Elvis, M., Schreier, E. J., Tonry, J., Davis, M., & Huchra, J. P. 1981, ApJ, 246, 20
Erlund, M. C., Fabian, A. C., Blundell, K. M., Celotti, A., & Crawford, C. S. 2006, MNRAS, 371, 29
Evans, D. A., Worrall, D. M., Hardcastle, M. J., Kraft, R. P., & Birkinshaw, M. 2006, ApJ, 642, 96
Fabbiano, G., Trinchieri, G., Elvis, M., Miller, L., & Longair, M. 1984, ApJ, 277, 115
Fabian, A. C., Celotti, A., & Johnstone, R. M. 2003a, MNRAS, 338, L7
Fabian, A. C., Crawford, C. S., Ettori, S., & Sanders, J. S. 2001, MNRAS, 322, L11
Fabian, A. C., Sanders, J. S., Crawford, C. S., & Ettori, S. 2003b, MNRAS, 341, 729
Falcke, H., Gopal-Krishna, & Biermann, P. L. 1995, A&A, 298, 395
Fanaroff, B. L., & Riley, J. M. 1974, MNRAS, 167, 31P
Fanti, C., Fanti, R., Parma, P., Schilizzi, R. T., & van Breugel, W. J. M. 1985, A&A, 143, 292
Fanti, C., Fanti, R., Parma, P., et al. 1989, A&A, 217, 44
Fernini, I., Burns, J. O., Bridle, A. H., & Perley, R. A. 1993, AJ, 105, 1690
Fernini, I., Burns, J. O., & Perley, R. A. 1997, AJ, 114, 2292
Fiore, F., Puccetti, S., Brusa, M., et al. 2009, ApJ, 693, 447
Fiore, F., Puccetti, S., Grazian, A., et al. 2012, A&A, 537, A16
Foley, A. R., & Barthel, P. D. 1990, A&A, 228, 17
Gambill, J. K., Sambruna, R. M., Chartas, G., et al. 2003, A&A, 401, 505
Gaskell, C. M., Goosmann, R. W., Antonucci, R. R. J., & Whysong, D. H. 2004, ApJ, 616, 147
Georgantopoulos, I., Dasyra, K. M., Rovilos, E., et al. 2011, A&A, 531, A116
Georgantopoulos, I., & Georgakakis, A. 2005, MNRAS, 358, 131
Ghisellini, G., & Celotti, A. 2001, A&A, 379, L1
Giavalisco, M., Ferguson, H. C., Koekemoer, A. M., et al. 2004, ApJL, 600, L93
Gilli, R., Comastri, A., & Hasinger, G. 2007, A&A, 463, 79
Gilli, R., Comastri, A., Vignali, C., Ranalli, P., & Iwasawa, K. 2010, in AIP Conf. Ser. 1248, X-ray Astronomy 2009: Present Status, Multi-Wavelength Approach and Future Perspectives, ed. A. Comastri, M. Cappi, & L. Angelini (Melville, NY: AIP), 359
Goulding, A. D., Alexander, D. M., Bauer, F. E., et al. 2012, ApJ, 755, 5
Grimes, J. A., Rawlings, S., & Willott, C. J. 2004, MNRAS, 349, 503
Grimes, J. A., Rawlings, S., & Willott, C. J. 2005, MNRAS, 359, 1345
Grogin, N. A., Kocevski, D. D., Faber, S. M., et al. 2011, ApJS, 197, 35
Haas, M., Müller, S. A. H., Bertoldi, F., et al. 2004, A&A, 424, 531
Haas, M., Siebenmorgen, R., Schulz, B., Krügel, E., & Chini, R. 2005, A&A, 442, L39
Haas, M., Willner, S. P., Heymann, F., et al. 2008, ApJ, 688, 122
Hardcastle, M. J., Evans, D. A., & Croston, J. H. 2009, MNRAS, 396, 1929
Hardcastle, M. J., Harris, D. E., Worrall, D. M., & Birkinshaw, M. 2004, ApJ, 612, 729
Hardcastle, M. J., & Worrall, D. M. 1999, MNRAS, 309, 969
Harris, D. E., & Krawczynski, H. 2006, ARA&A, 44, 463
Hasinger, G. 2008, A&A, 490, 905
Hes, R., Barthel, P. D., & Fosbury, R. A. E. 1993, Natur, 362, 326
Hickox, R. C., Jones, C., Forman, W. R., et al. 2007, ApJ, 671, 1365
Hine, R. G., & Longair, M. S. 1979, MNRAS, 188, 111
Hirst, P., Jackson, N., & Rawlings, S. 2003, MNRAS, 346, 1009
Hopkins, P. F., Hernquist, L., Cox, T. J., et al. 2006, ApJS, 163, 1
Hopkins, P. F., Hickox, R., Quataert, E., & Hernquist, L. 2009, MNRAS, 398, 333
Huchra, J., & Burg, R. 1992, ApJ, 393, 90
Iwasawa, K., Gilli, R., Vignali, C., et al. 2012, A&A, 546, A84
Jackson, N., & Browne, I. W. A. 1990, Natur, 343, 43
Jackson, N., & Rawlings, S. 1997, MNRAS, 286, 241
Juneau, S., Dickinson, M., Alexander, D. M., & Salim, S. 2011, ApJ, 736, 104
Just, D. W., Brandt, W. N., Shemmer, O., et al. 2007, ApJ, 665, 1004
Kim, M., Kim, D.-W., Wilkes, B. J., et al. 2007, ApJS, 169, 401
Koekemoer, A. M., Faber, S. M., Ferguson, H. C., et al. 2011, ApJS, 197, 36
Konigl, A., & Kartje, J. F. 1994, ApJ, 434, 446
Krolik, J. H., & Begelman, M. C. 1988, ApJ, 329, 702
Kuraszkiewicz, J., Wilkes, B. J., Schmidt, G., et al. 2009a, ApJ, 692, 1143
Kuraszkiewicz, J., Wilkes, B. J., Schmidt, G., et al. 2009b, ApJ, 692, 1180
La Franca, F., Fiore, F., Comastri, A., et al. 2005, ApJ, 635, 864
Laing, R. A., Riley, J. M., & Longair, M. S. 1983, MNRAS, 204, 151
Larson, D., Dunkley, J., Hinshaw, G., et al. 2011, ApJS, 192, 16
Laskar, T., Fabian, A. C., Blundell, K. M., & Erlund, M. C. 2010, MNRAS, 401, 1500
Law-Green, J. D. B., Leahy, J. P., Alexander, P., et al. 1995, MNRAS, 274, 939
Lawrence, A. 1991, MNRAS, 252, 586
Lawrence, A., & Elvis, M. 1982, ApJ, 256, 410
Lawrence, A., & Elvis, M. 2010, ApJ, 714, 561
Leipski, C., Haas, M., Willner, S. P., et al. 2010, ApJ, 717, 766
Liu, R., Pooley, G., & Riley, J. M. 1992, MNRAS, 257, 545
Longair, M. S. 1975, MNRAS, 173, 309
Lonsdale, C. J., & Barthel, P. D. 1984, A&A, 135, 45
Lonsdale, C. J., Barthel, P. D., & Miley, G. K. 1993, ApJS, 87, 63

Lonsdale, C. J., Smith, H. E., Rowan-Robinson, M., et al. 2003, PASP, 115, 897
Ludke, E., Garrington, S. T., Spencer, R. E., et al. 1998, MNRAS, 299, 467
Maiolino, R., Marconi, A., Salvati, M., et al. 2001, A&A, 365, 28
Maiolino, R., & Rieke, G. H. 1995, ApJ, 454, 95
Mantovani, F., Junor, W., Fanti, R., et al. 1992, MNRAS, 257, 353
Martínez-Sansigre, A., Rawlings, S., Lacy, M., et al. 2005, Natur, 436, 666
Matt, G., Fabian, A. C., Guainazzi, M., et al. 2000, MNRAS, 318, 173
Matt, G., Guainazzi, M., Frontera, F., et al. 1997, A&A, 325, L13
Monier, R., & Halpern, J. P. 1987, ApJL, 315, L17
Mulchaey, J. S., Koratkar, A., Ward, M. J., et al. 1994, ApJ, 436, 586
Murray, N., & Chiang, J. 1995, ApJL, 454, L105
Mushotzky, R. F., Done, C., & Pounds, K. A. 1993, ARA&A, 31, 717
Nenkova, M., Sirocky, M. M., Nikutta, R., Ivezić, Ž., & Elitzur, M. 2008, ApJ, 685, 160
O'Dea, C. P. 1998, PASP, 110, 493
Ogle, P., Whysong, D., & Antonucci, R. 2006, ApJ, 647, 161
Ogle, P. M., Brookings, T., Canizares, C. R., Lee, J. C., & Marshall, H. L. 2003, A&A, 402, 849
Oliver, S. J., Bock, J., Altieri, B., et al. 2012, MNRAS, 424, 1614
Orr, M. J. L., & Browne, I. W. A. 1982, MNRAS, 200, 1067
Panessa, F., Bassani, L., Cappi, M., et al. 2006, A&A, 455, 173
Park, T., Kashyap, V. L., Siemiginowska, A., et al. 2006, ApJ, 652, 610
Polletta, M., Weedman, D., Hönig, S., et al. 2008, ApJ, 675, 960
Polletta, M. d. C., Wilkes, B. J., Siana, B., et al. 2006, ApJ, 642, 673
Pounds, K., & Vaughan, S. 2006, MNRAS, 368, 707
Pounds, K. A., Wilkes, B. J., & Page, K. L. 2005, MNRAS, 362, 784
Ptak, A., Zakamska, N. L., Strauss, M. A., et al. 2006, ApJ, 637, 147
Rawlings, S., Lacy, M., Leahy, J. P., et al. 1996, MNRAS, 279, L13
Risaliti, G., Maiolino, R., & Salvati, M. 1999, ApJ, 522, 157
Salvati, M., Risaliti, G., Véron, P., & Woltjer, L. 2008, A&A, 478, 121
Sanders, D. B., Soifer, B. T., Elias, J. H., et al. 1988, ApJ, 325, 74
Sazonov, S., Willner, S. P., Goulding, A. D., et al. 2012, ApJ, 757, 181
Scoville, N., Aussel, H., Brusa, M., et al. 2007, ApJS, 172, 1
Seward, F. D. 2000, in Allen's Astrophysical Quantities, X-Ray Astronomy, ed. A. N. Cox (4th edition; New York, NY: Springer-Verlag), 183
Shi, Y., Rieke, G. H., Hines, D. C., et al. 2005, ApJ, 629, 88
Shi, Y., Rieke, G. H., Hines, D. C., et al. 2006, ApJ, 653, 127
Siemiginowska, A., Burke, D. J., Aldcroft, T. L., et al. 2010, ApJ, 722, 102
Siemiginowska, A., Cheung, C. C., LaMassa, S., et al. 2005, ApJ, 632, 110
Siemiginowska, A., LaMassa, S., Aldcroft, T. L., Bechtold, J., & Elvis, M. 2008, ApJ, 684, 811
Simpson, C. 2005, MNRAS, 360, 565
Singal, A. K. 1993, MNRAS, 262, L27
Spencer, R. E., Schilizzi, R. T., Fanti, C., et al. 1991, MNRAS, 250, 225
Tadhunter, C., Dicken, D., Holt, J., et al. 2007, ApJL, 661, L13
Tengstrand, O., Guainazzi, M., Siemiginowska, A., et al. 2009, A&A, 501, 89
Tozzi, P., Gilli, R., Mainieri, V., et al. 2006, A&A, 451, 457
Treister, E., Krolik, J. H., & Dullemond, C. 2008, ApJ, 679, 140
Treister, E., & Urry, C. M. 2006, ApJL, 652, L79
Trump, J. R., Impey, C. D., Taniguchi, Y., et al. 2009, ApJ, 706, 797
Whysong, D., & Antonucci, R. 2004, ApJ, 602, 116
Wilkes, B. J., & Elvis, M. 1987, ApJ, 323, 243
Wilkes, B. J., Lal, D. V., Worrall, D. M., et al. 2012, ApJ, 745, 84
Wilkes, B. J., Pounds, K. A., Schmidt, G. D., et al. 2005, ApJ, 634, 183
Wilkes, B. J., Schmidt, G. D., Cutri, R. M., et al. 2002, ApJL, 564, L65
Willott, C. J., Rawlings, S., Blundell, K. M., & Lacy, M. 2000, MNRAS, 316, 449
Wilman, R. J., & Fabian, A. C. 1999, MNRAS, 309, 862
Worrall, D. M. 2009, A&ARv, 17, 1
Worrall, D. M., & Birkinshaw, M. 1994, ApJ, 427, 134
Worrall, D. M., Lawrence, C. R., Pearson, T. J., & Readhead, A. C. S. 1994, ApJL, 420, L17
Worrall, D. M., & Wilkes, B. J. 1990, ApJ, 360, 396
Zakamska, N. L., Gómez, L., Strauss, M. A., & Krolik, J. H. 2008, AJ, 136, 1607
Zamorani, G., Henry, J. P., Maccacaro, T., et al. 1981, ApJ, 245, 357
Zirm, A. W., Dickinson, M., & Dey, A. 2003, ApJ, 585, 90